Kaunas University of Technology

Faculty of Mathematics and Natural Sciences

Development of Gd_2O_3 reinforced polymeric 3D printing materials for radiation shielding

Master's Final Project

Project prepared by

Yan Tung Lai

Project supervisor

Prof. Dr. Diana Adlienė

Kaunas, 2026

Kaunas University of Technology

Faculty of Mathematics and Natural Sciences

Development of Gd_2O_3 reinforced polymeric 3D printing materials for radiation shielding

Master's final project

Medical Physics (6213GX001)

Project prepared by

Yan Tung Lai

Project supervisor

Prof. Dr. Diana Adlienė

Project reviewed by

Matas Bašinskas

Kaunas, 2026

Kaunas University of Technology

Faculty of Mathematics and Natural Sciences

Yan Tung Lai

Development of Gd_2O_3 reinforced polymeric 3D printing materials for radiation shielding

Declaration of academic integrity

I confirm that:

1. I have prepared this final project independently and honestly, without violating the copyright or other rights of other persons, in compliance with the Law on Copyright and Related Rights of the Republic of Lithuania, the provisions of Kaunas University of Technology (hereinafter referred to as the University) on the management and transfer of intellectual property, and the ethical requirements set out in the University's Code of Academic Ethics;

2. All data and research results presented in the final project are accurate and obtained legally, no part of the project has been plagiarized from printed or electronic sources, and all quotations and references presented in the text of the final project are indicated in the list of references;

3. I have complied with personal data protection requirements in the final project, have not used undisclosed or confidential data without legal grounds, and if I have used such data, it has been properly anonymized;

4. If I used artificial intelligence (hereinafter referred to as AI) or other automated tools in preparing the final project, I applied them in accordance with the procedures established by the University, without violating the principles of academic integrity.

5. I have not paid and am not obliged to pay any sums of money not provided for by law for the final project or any part thereof to any natural or legal person;

6. I understand that if academic dishonesty or violation of other persons' rights is discovered, I will be held accountable in accordance with the procedures established by the University and may be expelled from the University; cases of academic dishonesty may be investigated even after graduation, initiating the procedure for revoking the degree.

Lai, Yan Tung. Gd_2O_3 praturtintų polimerinių 3D spausdinimo medžiagų kūrimas apsaugai nuo spinduliuotės. Magistro baigiamasis projektas rojekto vadovė prof. dr. Diana Adlienė; Kauno technologijos universitetas, Matematikos ir gamtos mokslų fakultetas.

Sudijų kryptis ir studijų krypties grupė: Medicinos technologijos G09, Sveikatos mokslai.

Raktažodžiai: neutronų ekranavimas, 3D spausdinimas, 3D spausdinimo medžiagos.

Kaunas, 2026. p.62.

Santrauka

Radiacijos slopinimas medicinos įrenginiuose, naudojant bešvinius ekranavimo elementus, pagamintus iš polimerinių kompozitų, pastaruoju metu sulaukia vis daugiau dėmesio. Kadangi tokiuose įrenginiuose, kaip linijinis greitintuvas, pasireiškia mišri neutroninė ir fotoninė spinduliuotė, veiksmingam ekranavimui būtinas dviejų etapų principas: pirmiausia greitieji neutronai turi būti sulėtinti iki šiluminių neutronų, o vėliau turi būti sugeriami šiluminiai neutronai ir didelės energijos fotonai. Didelio tankio polietilenas (HDPE) yra gerai žinomas polimeras, kuris efektyviai moderuoja neutronus, nes savo sudėtyje turi daug vandenilio, kuris lėtina greituosius neutronus vyskstant elastinei sklaidai. Gd_2O_3 pasižymi geromis šiluminių neutronų ir didelės energijos fotonų slopinimo savybėmis, nes turi didelį neutronų sugerties skerspjūvį ir yra veiksmingas įvairiuose fotonų sąveikos procesuose, tokiuose kaip fotoelektrinis efektas ar Komptono sklaida.

Šiame darbe siekiama ištirti Gd_2O_3 praturtintų HDPE kompozitų gebėjimą slopinti mišriąją spinduliuotę. Įgyvendinant šį tikslą, naudojant 3Devo Precision ekstruzijos įrangą, buvo pagamintos trijų rūšių kompozitinės skaidulos, skirtos 3D spausdinimui: gryno HDPE, HDPE su 5 wt.% Gd_2O_3 ir HDPE su 10 wt.% Gd_2O_3. Iš pagamintų skaidulų naudojant 3D spausdintuvą Creality K2 Plus 3D buvo pagaminti 2 tipų bandiniai: cilindriniai (skersmuo – 20 mm, storis – 5 mm), skirti spinduliuotės slopinimo efektyvumui vertinti, o taip pat ISO 527-2 1BA („šuns kaulo“ tipo) bandiniai, skirti kompozitų mechaninių savybių testavimui.

Bandinių apšvitai buvo naudojamas mišrios (neutronų ir gama) Pu-Be šaltinis, kur neutronų srautas sudarė 6.85×10^4 n/cm²/s. Apšvita vykdyta Fizinių ir technologijos mokslų centro branduolinių tyrimų skyriuje. Polimerinių kompozitų efektyvumas slopinant mišriąją spinduliuotę buvo įvertintos naudojant Gafchromic™ EBT3 dozimetrines plėveles. Polimerinių kompozitų mechaninės savybės buvo tiriamos naudojant universalią mechaninio testavimo įrangą Tinius Olsen H25 KT (Tinius Olsen, Horsham, United States).

Gauti rezultatai rodo, kad varijuojant 3D spausdinamo HDPE + Gd_2O_3 kompozito struktūrų storį ir priedų koncentracijas, jos yra perspektyvios vystant lengvas, bešvines mišrios spinduliuotės (neutronai+fotonai) ekranavimo konstrukcijas medicinoje.

Lai, Yan Tung. Development of Gd_2O_3 reinforced polymeric 3D printing materials for radiation shielding. Master's Final Degree Project / supervisor prof. dr., Diana Adlienė; Faculty of Mathematics and Natural Sciences, Kaunas University of Technology.

Field of study and field of study group: Medical Technologies G09, Health sciences.

Keywords: neutron shielding, 3D printing, 3D printing materials.

Kaunas, 2026. 62.

Summary

Radiation shielding in LINAC head with lead free and polymer composite materials has drawn attention in the medical physics field. An effective two stage shielding approach is needed, including the moderation of fast neutrons into thermal neutrons, followed by the absorption of thermal neutrons and high-energy photon radiation. HDPE is recognized as an effective neutron moderator due to its high hydrogen content, which effectively slows-down fast neutron through elastic scattering. On the other hand, Gd2O3 has strong attenuation capability for both thermal neutrons and photons, owing to its high neutron capture cross section and its effectiveness in photon interactions such as the photoelectric effect and Compton scattering.

Therefore, this report aims to investigate the shielding performance of 3D printed HDPE composites reinforced with Gd_2O_3. Three types of filaments, HDPE, HDPE/5 wt% Gd_2O_3, and HDPE/10 wt% Gd_2O_3 were successfully produced using a 3Devo Precision filament extruder, and corresponding samples were fabricated with a Creality K2 Plus 3D printer. The produced filaments were used to print cylindrical samples with a diameter of 20 mm and a thickness of 5 mm, and the test specimens - ISO 527-2 type 1BA for attenuation test and tensile test, respectively. A Pu-Be mixed field radiation neutron source with a neutron flux 6.85×10^4 n/cm^2/s was used for sample irradiation, which was performed at the Center of Physical and Technological Sciences, Department of Nuclear Research. The attenuation properties, including mean neutron transmission and attenuation percentage values, were analyzed using GafchromicTM EBT3 film as dosimetry tool for data collection. A universal testing machine (UTM) Tinius Olsen H25 KT (Tinius Olsen, Horsham, United States), was used to test mechanical properties of 3D printed composites.

The obtained results indicate that 3D-printed HDPE/Gd_2O_3 composite structures with different filler concentrations may be promising candidates for the development of lightweight, lead-free shielding materials against mixed radiation fields, including neutrons and photons. Such materials could be particularly relevant for localized shielding applications in medical linear accelerator heads, where photoneutron production requires compact and adaptable radiation protection solutions.

Contents

List of tables 7
List of figures 8
List of abbreviations and terms 10
Introduction 11
1. Literature Review 12
1.1. Linear accelerator 12
1.1.1. Structure of the LINAC head 12
1.1.2. Photoneutron production 14
1.1.3. Radiation leakage problem 17
1.1.4. Side effect of LINAC head leakage to patient 20
1.2. Neutron shielding mechanism 21
1.3. Experimental setup 25
1.3.1. 3D Printing methods 25
1.3.2. Dosimetry 26
2. Materials and methods 31
2.1. Filament production 31
2.2. 3D printing 33
2.2.1. Sample and test specimens design 35
2.2.2. Magigoo PP glue application 37
2.3. Mechanical test 37
2.3.1. Tensile test methodology 37
2.3.2. Theoretical calculations of attenuation properties 38
2.3.3. Experimental setup of attenuation test 39
3. Result and discussion 42
3.1. Filament production 42
3.2. 3D printed result of samples and test specimen 44
3.3. Mechanical tests 49
3.3.1. Tensile test 49
3.3.2. Theoretical radiations attenuation properties 52
3.3.3. Attenuation properties of experimental samples 55
Conclusions 57
List of references 58

List of tables

Table 1. Advantages and disadvantages of different type photon detector..... 27
Table 2. Characteristics of HDPE granules and Gd_2O_3 powder..... 31
Table 3. HDPE-based composites' formula by weight..... 38
Table 4. Extruded filaments' characteristics..... 42
Table 5. Extruder's parameters in filament production..... 43
Table 6. 3D printing parameters in different materials..... 44
Table 7. Fans speed setting for 3D printing..... 45
Table 8. Illustration of adjustment process of 3D printing HDPE/5%Gd_2O_3 samples..... 46
Table 9. Illustration of adjustment process of 3D printing HDPE test specimens..... 47
Table 10. Comparison between theoretical density and measured density..... 48
Table 11. Tensile test result..... 50

List of figures

Fig. 1. Structure of the LINAC head (Miyasaka et al., 2021) 13
Fig. 2. Beam without flattening filter in LINAC(left), and with flattering filter(right) (Alex et al., 2013) 13
Fig. 3. Materials used in LINAC head components (S. Agustín, 2013) 15
Fig. 4. The radionuclides emitted from the LINAC head (M.F. Uddin et al., 2024) 16
Fig. 5. Photoneutron production in different metals used in the LINAC head (Facure et al., 2008) 16
Fig. 6. Photoneutron spectra of LINAC accelerators in 15MeV (Howell et al., 2009) 17
Fig. 7. Mean neutron energies leaked from different components of the LINAC head (H. Brkić et al., 2018) 18
Fig. 8. Neutron spectra from LINAC head simulation results at three points of interest (H. Brkić et al., 2018) 18
Fig. 9. The measured position of LINAC radiation leakage in horizontal (left), and vertical (right) beam direction (T. Almatani and R.P. Hugtenburg, 2025) 19
Fig. 10. Neutron leakage measurement from LINAC head at multiple angles (T. Almatani and R.P. Hugtenburg, 2025) 20
Fig. 11. Summary of the neutron ambient dose equivalent induced by different LINAC machines (Kry et al., 2017) 21
Fig. 12. Experimental mass attenuation coefficient results of HDPE reinforced with Gd_2O_3 fillers at different concentrations (M. Shabib et al., 2026) 22
Fig. 13. The Gd2O3/HDPE composites' total macroscopic cross section value plot (M. Shabib et al., 2026) 23
Fig. 14. Fast neutron removal cross section for HDPE/oxide composites (A. Alharbi et al., 2026) 23
Fig. 15. Plots of mass attenuation coefficient against photon energy of rare-oxides/HDPE composites (K. Saenboonruang et al., 2021) 24
Fig. 16. 3D printing technologies classification (H. Alamei et al., 2022) 25
Fig 17. Experimental setup for investigating neutron shielding properties (Z. Uddin et al., 2020) 28
Fig. 18. The bubble detector (E. Ramalho et al., 2011) 29
Fig. 19. The Gd2O3 geometry (A. Ayuela et al., 2007) 31
Fig. 20. 3Devo filament extruder 32
Fig. 21. Heater zones in the extruder 32
Fig. 22. Castor oil (left), mixed material (middle), mixed material in extruder (right) 33
Fig. 23. Creality K2 Plus 3D printer (left), and the printing process (right) 34
Fig. 24. Modelling of test specimen in ISO 527-2 Type 1BA 35
Fig. 25. Standard tensile test specimen of ISO 527-2 Type 1BA and 1BB (BSI, 2012) 35
Fig. 26. Modelling of sample 36
Fig. 27. Glue (left), illustration of using the glue (right) 37
Fig. 28. Universal testing machine Tinius Olsen H25 KT machine(left), and the tensile test process(right) 38
Fig. 29. Shielded concrete construction with the central irradiation channel (left) and holder container with samples (right) 39
Fig. 30. Schematic of the structure of neutron sources 40

Fig. 31. Neutron spectrum of central channel 40
Fig. 32. HP Scanjet G4050 machine for scanning (left), and the process of film scanning (right) 41
Fig. 33. Filaments produced from the prepared composite materials. 42
Fig. 34. Spooling of HDPE filament 43
Fig. 35. Printed samples 48
Fig. 36. Printed test specimens of different materials 49
Fig. 37. Stress–strain curves of the printed HDPE-based composites before and after irradiation 49
Fig. 38. Young's modulus of the printed HDPE-based composites before and after irradiation 51
Fig. 39. NGCal simulation results of neutron mass attenuation 52
Fig. 40. Thermal neutron attenuation factor for HDPE/Gd_2O_3 composites 52
Fig. 41. Fast neutron parameters of HDPE/Gd_2O_3 composites 53
Fig. 42. Mass attenuation coefficient of HDPE/Gd_2O_3 composites 54
Fig. 43. Average transmission and attenuation percentage results of samples in EBT3 film 55
Fig. 44. Average attenuation percentage for printed HDPE/Gd_2O_3 composite samples ... 56

List of abbreviations and terms

FNRCS - Fast Neutron Removal Cross Section

IMRT – Intensity modulated radiation therapy

LINAC – Linear Accelerator

MLC - Multileaf Collimators

MC – Mont Carlo

VMAT – Volumetric arc therapy

Introduction

The linear accelerator (LINAC) is essential for cancer treatment nowadays, which delivers precise and high energy radiation (6 - 18 MeV) to cancerous tissue while sparing healthy organs. Treatment techniques such as intensity-modulated radiation therapy (IMRT) and volumetric modulated arc therapy (VMAT) are delivered by the LINAC for cancer treatment. However, leakage radiation from the LINAC head is one of the ongoing issues that still requires close attention. Unintended radiation escapes from the treatment head of the LINAC, which contributes unnecessary exposure to patients and personnel over time. There are several critical components in the LINAC head, including the target (radiation source), primary collimator, flattening filter, ionization chambers (monitor chamber), secondary collimator (jaws), and multileaf collimators (MLCs) [1]. They mainly made of tungsten, lead, aluminum, and iron and etc [2].

Photoneutrons are generated within the LINAC head when high-energy bremsstrahlung photons induce photonuclear interactions, commonly referred to as (γ,n) reactions. When the incident photon energy exceeds the nuclear binding energy of the constituent materials in the LINAC head, neutrons are ejected [3]. According to the research of Sohrabi, M. and Hakimi, A., photoneutrons production occurs when photon energy is higher than 6 MeV [4] and significant neutrons produced if photon energy is higher than 10 MeV [5]. Within the operating range of 10 to 24 MeV, photoneutrons emitted from LINAC head possess mean energies from 0.287 to 0.838 MeV [6]. The radiation leakage in the LINAC head affects patients, as they may be exposed to unwanted neutrons which can cause biological damage, and increase the possibility of radiation-induced secondary cancer [22].

The ALARA (As Low As Reasonably Achievable) approach can be implemented if suitable materials are used for room shielding and for LINAC head design. To attenuate the photoneutrons, materials should be able to minimize the peripheral dose (out-of-field dose). Although conventional high-Z shielding materials such as lead are highly effective for photon attenuation, they have limited neutron shielding capability. Therefore, HDPE/Gd_2O_3 composites were investigated in this report to address this limitation and improve shielding performance in mixed neutron–photon radiation fields. Polyethylene is effective for neutron moderation because of its high hydrogen content and effective removal cross-section. However, polyethylene is less effective for shielding thermal neutrons and high-energy photons because of its low thermal neutron capture cross-section and low atomic number. Therefore, polyethylene is often used in combination with high thermal neutron absorption capability and high-Z materials to improve thermal neutron and photon shielding performance. For example, using Gd_2O_3 filler, as many studies have indicated that the mass attenuation coefficient μ_m enhanced with increasing Gd_2O_3 filler concentration in low energy levels. Also, Gd is a strong neutron absorber, as increasing of Gd_2O_3 content enhances the probability of neutron interaction ($\sum_T$) [7].

1. Literature Review

Radiation shielding in the LINAC head using lead free and plastic composite materials has drawn attention in the medical physics field, to enhance the effectiveness of high-energy photons and secondary neutrons shielding. The current literature evaluates the radiation shielding effectiveness of HDPE-based composites by examining their manufacturing techniques, experimental testing methods, and overall performance in terms of both mechanical strength and radiation-blocking capability.

1.1. Linear accelerator

A LINAC is one of the medical devices used in radiation therapy, which is applied in the treatment of more than 50% of cancer patients [8]. It can operate in electron or photon modes based on the location of the tumor, with beam energies ranging from 6 MeV to 25 MeV [9].

There are three types of radiations produced by the LINAC that need to be considered by a physicist: primary radiation, scattered radiation, and leakage radiation [10]. Primary radiation refers to the main beam designed for cancer treatment and intentionally directed at the patient's tumor. Secondary radiation refers to the scattered radiation produced primary beam interacts with matter, such as patient's body, walls, and LINAC components. Leakage radiation refers to a fraction of unintended radiation released from the LINAC head when the machine is on, and it is not considered as part of the primary beam [11].

When medical linear accelerator facilities are implemented, radiation protection is achieved mainly through two strategies: structural room shielding and internal head shielding. The structural room shielding protects the external environment, corresponding to the primary and secondary barriers. NCRP Reports No. 49, 51, and 79 provide guidelines on the shielding design and barrier thickness calculations [10]. While the internal head shielding serves to protect personnel and patients in the room by reducing leakage radiation.

This report focused on addressing the leakage radiation from LINAC head.

1.1.1. Structure of the LINAC head

There are several critical components in the LINAC head used to deliver the radiation beam, including the target (radiation source), primary collimator, flattening filter, ionization chambers (monitor chamber), secondary collimator (jaws), and multileaf collimators (MLCs) (Fig. 1) [1].

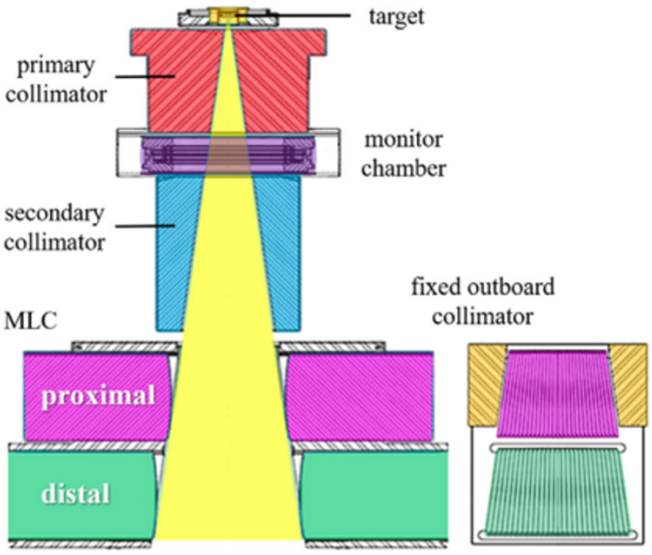

Fig. 1. Structure of the LINAC head (Miyasaka et al., 2021)

A LINAC generates high-energy radiation by accelerating electrons in a straight line using electromagnetic waves. The electrons, produced by an electron gun, are accelerated through a waveguide by microwaves from a magnetron or klystron. Magnetic fields focus and direct the beam toward the treatment head, where it strikes a tungsten target to produce X-rays through the Bremsstrahlung process.

Then, the X-ray passes through the primary collimator, which are in fixed position to determine the maximum amount and circular field size of the X-rays beam. The size of the beam is usually 40 x 40 cm at a 100cm distance to the source [12].

Next, the X-ray passes along the flattering filter, which is in a conical shape and is used to make the beam intensity more uniform, as shown in Fig. 2. Since the X-ray beam has the highest intensity in the center, the filter reduces the intensity of the central beam, resulting a flat and uniform beam distribution.

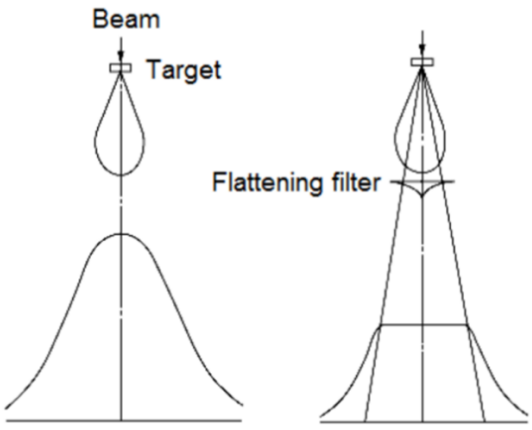

Fig. 2. Beam without flattening filter in LINAC(left), and with flattering filter(right) (Alex et al., 2013)

After that, the ionization chambers continuously monitor the radiation dose, ensuring a uniform, symmetric and steady beam delivery. The chambers initiated an auto beam cutoff if any deviations are detected [13].

After passing through the primary collimator and flattening filter, the X-ray beam passes through the secondary collimator system, commonly known as the jaws. The jaws are usually made of high-density materials such as tungsten or tungsten alloy to attenuate the radiation outside the treatment field. This system consists of two pairs of movable jaws: the X jaws and the Y jaws, which define the rectangular treatment field size. The jaw faces are designed to follow the divergence of the X-ray beam so that they remain approximately aligned with the beam edges. This helps reduce unnecessary transmission and scattering from the jaw surfaces. In many LINAC designs, the Y jaws move along a curved or arc-like path, while the X jaws move linearly. If the jaw faces are not correctly aligned with the divergent beam edge, the field shape, dose distribution, penumbra, and scattered radiation may be affected [14].

The multileaf collimators (MCLs) are located below the jaws and used for field shaping. They are usually made of tungsten alloy material. Figure 1 shows a Halcyon head which has double-layer MCLs, with a proximal layer containing 29 leaf pairs and a distal layer containing with 28 leaf pairs. Each leaf pair has the same travelling distance, moving at a certain speed to shape the field by adjusting the gap width. This is essential for IMRT and VMAT treatment planning, which affects the resolution and the quality of transmission [1]. Each LINAC model has its own MLCs design, which is slightly different from each other.

1.1.2. Photoneutron production

Photoneutrons are produced when high-energy photons undergo photonuclear interactions with high-Z materials in the LINAC head [3]. A report from AAPM 19 stated that neutrons are produced when the clinical LINAC operates at energies higher than 8 MeV [15]. However, studies by Sohrabi and Hakimi reported that photoneutron production can occur when photon energy exceeds 6 MeV [4], while significant neutron production occurs at photon energies higher than 10 MeV [5]. NCRP Report No. 151 stated that, for a LINAC operating at 15 MeV, the maximum emitted neutron energy can reach up to 10 MeV. However, the average neutron energy is typically about 1–2 MeV, which requires special room design considerations for neutron shielding [16].

To understand more about the materials contained in each component in the LINAC head, S. Agustín studied [2] four different LINAC machines, explaining the elements and densities in each component, with LINAC brands including Siemens KDS, Elekta Inor, Elekta SL25, and Varian LINAC. Research has shown that the collimators and jaws are usually made of tungsten, lead, and iron. In some LINAC designs, copper is used as shielding material in the target region, while the flattening filter may be made of different materials depending on the beam energy and LINAC design. When the high-energy photons interact with all these high-Z materials and exceed the minimum threshold energy, neutrons are produced due to the (γ, n) reaction. They stated that the material utilized in the LINAC head and its associated threshold for photonuclear reactions determines the amount of neutrons produced. The

threshold energies of tungsten, lead, aluminum, and iron are 6.2, 6.7, 13.1, and 7.6 MeV respectively [2].

		Siemens KDS	Elekta Inor	Elekta SL25	Varian Clinac	
		18 MV	15MV	18 MV	15 MV	18/20 MV
target	materials	Au	W/Re	W/Ni/Fe	W	
	[%]	100	90/10	95/3.75/1.25	100	
	ρ [g cm^{-3}]	19.3	19.4	18.0	19.3	
target cover	materials	Cu	Cu		Cu	
	[%]	100	100		100	
	ρ [g cm^{-3}]	8.96	8.96		8.96	
primary collimator	materials	W	W/Ni/Fe	Pb/Sb	W	
	[%]	100	95/3.75/1.25	96/4	100	
	ρ [g cm^{-3}]	19.3	18.0	11.12	19.3	
flattening filter	materials	Cr/Fe/Ni	Cr/Ni/Fe		W	Ta/Fe
	[%]	18/74/8	18/74/8		100	–
	ρ [g cm^{-3}]	8.03	8.03		19.3	16.65/7.874
secondary collimator	materials	W	W/Ni/Fe	Pb/Sb	W	
	[%]	100	95/3.75/1.25	96/4	100	
	ρ [g cm^{-3}]	19.3	18.0	11.12	19.3	
multileaf collimator	materials		W/Ni/Fe	Pb/Sb	W	
	[%]		95/3.75/1.25	96/4	100	
	ρ [g cm^{-3}]		18.0	11.12	19.3	
jaws	materials	W	W/Ni/Fe	Pb/Sb	W	
	[%]	100	95/3.75/1.25	96/4	100	
	ρ [g cm^{-3}]	19.3	18.0	11.12	19.3	

Fig. 3. Materials used in LINAC head components (S. Agustín, 2013)

The neutron spectrum and bremsstrahlung production are usually calculated by the Monte Carlo (MC) simulations [17,18]. In the study by C. Besnard-Vauterin et al., FLUKA, Geant4, MCNP6, and PHITS codes were used for neutron spectrum simulation. As a result, the emitted neutron energy can be approximately calculated according to equation (1) [17]:

$$E_n = \frac{E_\gamma - Q - E_{state}}{1 + A_{residual}^{-1}}, \quad (1)$$

where E_γ - the incident energy of photon produced by the LINAC;

Q - reaction value;

E_{state} - residual nucleus's excited state energy;

$A_{residual}$ - residual nucleus's mass number.

Neutrons can be generated through photonuclear reactions induced by high-energy bremsstrahlung photons, commonly known as (γ,n) reactions. When high-energy electrons strike the target, bremsstrahlung X-rays are emitted. If the X-ray photon energy is high enough, these photons can interact with atomic nuclei and eject neutrons. In the clinically relevant energy range, this process is mainly explained by the giant dipole resonance (GDR), where protons and neutrons in the nucleus oscillate against each other. This nuclear excitation can result in neutron emission After being produced, the emitted neutrons can interact with materials inside the LINAC head and treatment room, forming unstable radioactive isotopes. These isotopes may decay by emitting beta and/or gamma radiation with specific energies and half-lives [8]. This process can be simply represented by the following equation (2):

$$\gamma + A \rightarrow (A-1) + n \quad (2)$$

In M.F. Uddin et al. research, the produced radionuclides were shown after the elements in the LINAC head became activated, including aluminum, copper, manganese, nickel, and tungsten. Beta-minus particles are emitted when neutron-rich isotopes are formed, such as when Manganese-55 absorbs a neutron and becomes Magganese-56. In contrast, positron emission can occur when proton-rich isotopes are produced, for example when copper-62 is formed from copper-63 through the photonuclear reaction $^{63}Cu(\gamma,n)^{62}Cu$ (fig. 4) [19]. Figure 4 shows that the highest emitted photon energy can be up to 1920 for keV by nickel, followed by 1779 keV for aluminum and 1346 keV for copper.

Radionuclides produced in medical accelerators.

Activation process	Decay mechanism	Half-life	Photon energy (keV)	Photonuclear threshold activated (MeV)
$^{27}Al\ (n, \gamma)^{28}Al$	β^-	2.3 m	1779	–
$^{63}Cu\ (\gamma, n)^{62}Cu$	β^+	9.74 m	511	10.85
$^{55}Mn\ (n, \gamma)^{56}Mn$	β^-	2.6 h	847	10.23
$^{65}Cu\ (\gamma, n)^{64}Cu$	β^+, β^-	12.7 h	1346	9.91
$^{58}Ni\ (\gamma, n)^{57}Ni$	β^+	35.0 h	1378, 1920	12.22
$^{186}W\ (n, \gamma)^{187}W$	β^-	23.9 h	479, 686	–

Fig. 4. The radionuclides emitted from the LINAC head (M.F. Uddin et al., 2024)

Neutron production is highly related to the element, and high-Z materials can produce neutrons more easily. For example, tungsten-186 only requires 5.75 MeV to knock out a neutron, compared to tungsten-182, which requires 8.50 MeV (Fig. 5). Also, the higher the isotope abundance, the higher the probability of neutron production [20].

Element	Atomic weight	Abundance (%)	Threshold energy (MeV)
Al	27	100	13.10
Fe	54	5.8	13.40
	56	91.7	11.20
Cu	65	30.8	9.91
W	182	26.4	8.50
	183	14.4	6.19
	184	30.6	7.41
	186	28.4	5.75
Pb	206	25.1	8.08
	207	22.1	6.74
	208	52.3	7.37

Fig. 5. Photoneutron production in different metals used in the LINAC head (Facure et al., 2008)

In general, tungsten, aluminum, copper, lead, and iron are major sources of induced neutron in the LINAC head. Tungsten, copper, and lead have relatively lower threshold energies to produce neutrons, as they have higher atomic weights.

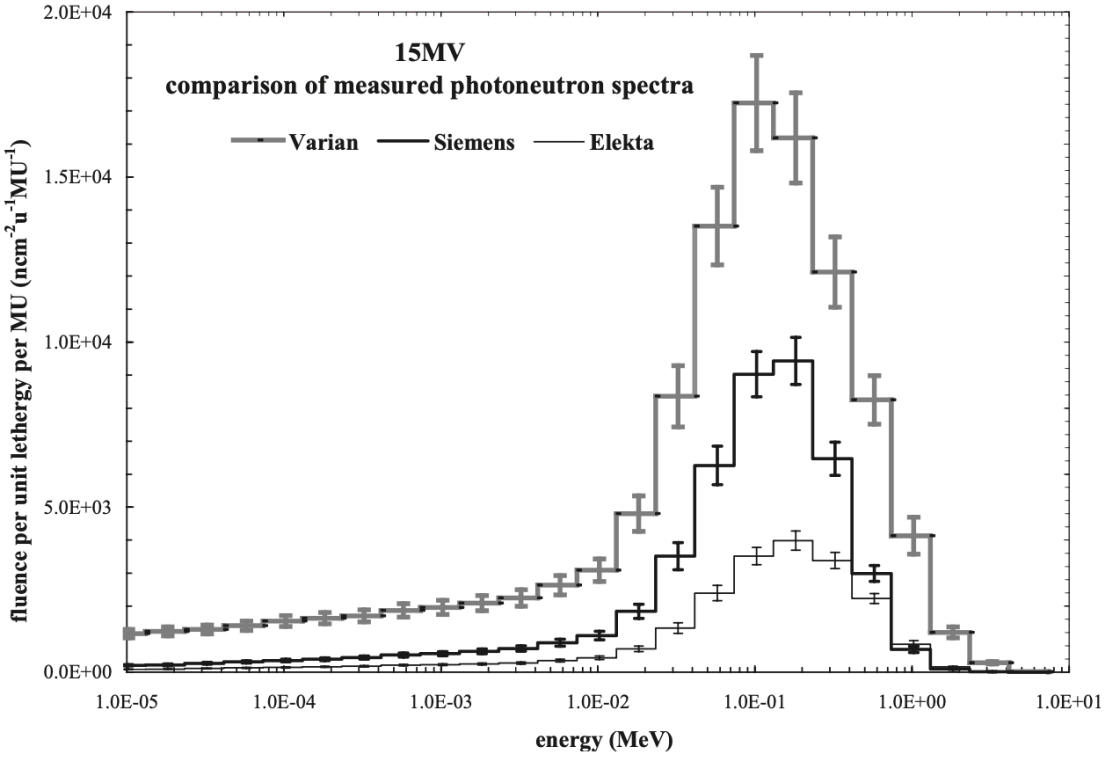

Fig. 6. Photoneutron spectra of LINAC accelerators in 15MeV (Howell et al., 2009)

The measured photoneutron spectra for 15MeV LINAC accelerators (Varian, Siemens, and Elekta) are shown in Figure 6. The results indicate that the Varian accelerator exhibits the highest neutron fluence in the neutron energy region around 0.1 MeV, followed by Siemens and Elekta accelerators. The investigation showed a similar general trend, characterized by the highest fluence value around 0.1 MeV, and relatively low fluence values below 0.001MeV and over 1MeV. Beyond the peak energy, the neutron fluence decreases significantly toward higher energies [21].

1.1.3. Radiation leakage problem

Measurement and regulation of the LINAC head's radiation leakage are important for patient and staff safety. Unlike primary radiation, leakage radiation is unwanted radiation that may expose patients without providing any therapeutic benefit. NCRP Report 49 established a regulatory threshold, restricting the leakage radiation to less than 0.1% of the primary beam intensity at 1 m from the radiation source [16].

Radiation leakage from the LINAC head is caused by the inefficient attenuation of high-energy photons and photoneutrons by the internal shielding components. Some radiation escapes or scatters through internal parts despite the strong shielding of the LINAC head.

H. Brkić et al. studied (Figure 7) the amount of neutron leakage from different components of the LINAC head using Monte Carlo (MC) simulations. They analyzed components, including the head cover (HC), primary collimator (PC), flattening filter (FF), monitor chamber (MC), jaws, and target (Fig. 7). They compared the results for two different modes, full mode (with phantom) and empty mode (without phantom), in three different locations of interest: isocenter, above, and lateral positions ("aside") [22].

	Energy [MeV]						
	HC	PC	FF	MC	Jaws	Target	Overall
	Full						
Isocenter	0.27	0.77	1.06	0.29	0.40	1.03	0.55
Above	0.36	0.55	0.79	0.14	0.38	0.69	0.50
Aside	0.38	0.51	0.55	0.19	0.47	0.55	0.46
	Empty						
Isocenter	0.00	0.84	0.90	0.25	0.43	1.10	0.59
Above	0.00	0.74	0.95	0.21	0.42	0.90	0.71
Aside	0.00	0.75	0.89	0.39	0.69	0.96	0.75

Fig. 7. Mean neutron energies leaked from different components of the LINAC head (H. Brkić et al., 2018)

The study found that higher neutron energies were produced in the target, flattening filter and primary collimator. Lower neutron energies were produced in the head cover and jaws. For the neutrons reaching the isocenter in both modes, there was little variation. However, at other two locations of interest (above and lateral to the LINAC head), the empty mode showed higher neutron leakage compared to the full mode. This is because the empty mode did not include a phantom, which could attenuate or scatter some neutrons before they reached the detectors [22].

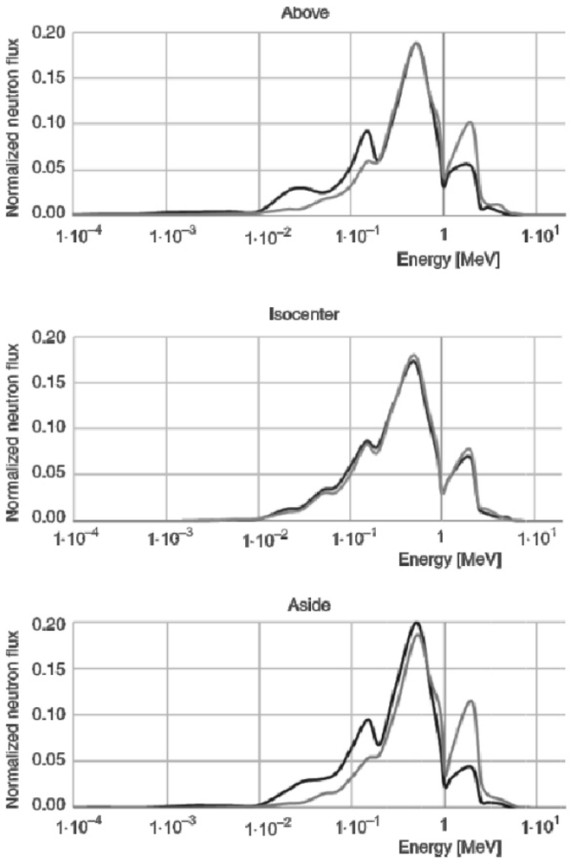

Fig. 8. Neutron spectra from LINAC head simulation results at three points of interest (H. Brkić et al., 2018)

Figure 8 shows the comparison of neutron spectra of the LINAC head in full mode (black line) and in empty mode (grey line), in which more neutrons with relatively lower energy were observed in full mode for all the points of interest. Also, their simulation indicated that the peak neutron flux occurred in the 0.1–0.5 MeV energy range for all points of interest.

One of the other discussions was that the area around the LINAC head had higher neutron contamination than the patient plane. This suggests that personnel working near the LINAC head during daily operation may be exposed to unnecessary radiation [22].

Also, radiation leakage from the LINAC head can be distributed non-uniformly in all directions. A study from T. Almatani and R.P. Hugtenburg [11] investigated the leakage problem in the LINAC head through different ranges and angles. They then compared the experimental results with FLUKA MC simulation results obtained for a 6 MeV photon beam irradiated in two directions: vertical, toward the patient plane, and horizontal. For horizontal beam irradiation, the measurement positions were 45°, 90°, 135°, and 180°, while for vertical beam irradiation, they were 270°, 180°, 90°, and 0°. They found that the isocenter had the highest leakage measurement, followed by the backscattering at the 180° position when the irradiation beam directed horizontally, while the highest radiation leakage was obtained at 180° position when the irradiation beam directed vertically. At almost all angles and geometries around the LINAC head, radiation leakage was observed at different levels.

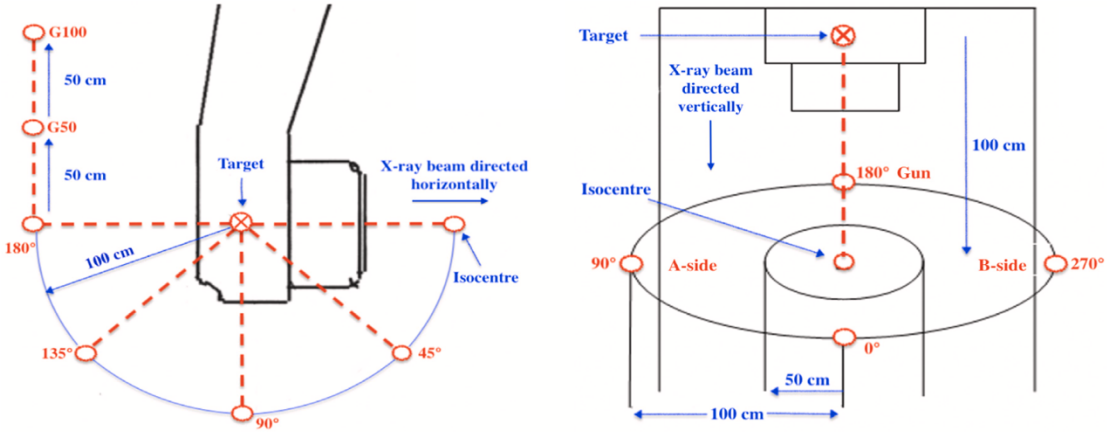

Fig. 9. The measured position of LINAC radiation leakage in horizontal (left), and vertical (right) beam direction (T. Almatani and R.P. Hugtenburg, 2025)

A TK-30 spherical ionization chamber with a 27.9 cm^3 sensitivity volume was used. Also, the percentage results shown in Figure 10 were normalized to the references dose at the isocenter.

Leakage measurement positions when the beam is directed horizontally.

Chamber position	Leakage (%)		MC statistical uncertainty (%)
	Measurement	MC simulation	
G100	0.03	0.023	16
G50	0.05	0.047	13
180°	0.06	0.068	10
135°	0.05	0.045	14
90°	0.02	0.036	11
45°	0.01	0.016	20
Isocentre	0.547	0.576	6

Leakage measurement positions when the beam is directed vertically.

Chamber position	Radius	Leakage (%)		MC statistical uncertainty (%)
		Measurement	Simulation	
90° (A-side)	50 cm	0.02	0.025	14
90° (A-side)	100 cm	0.02	0.008	18
0°	50 cm	0.01	0.013	22
0°	100 cm	0.01	0.024	23
270° (B-side)	50 cm	0.02	0.021	19
270° (B-side)	100 cm	0.02	0.006	30
180° (Gun)	50 cm	0.03	0.021	18

Fig. 10. Neutron leakage measurement from LINAC head at multiple angles (T. Almatani and R.P. Hugtenburg, 2025)

To shield all the radiation leakage, they calculated and estimated that the lead shield thickness range should be from 6.8 to 13.6 cm at different positions around the LINAC head. They concluded that the FLUKA MC mode was trustworthy, with high simulation as compared to the experimental measurement result, only having -1.2% mean difference.

In summary, both H. Brkić et al. [22] and T. Almatani and R. P. Hugtenburg [11] concluded that the highest radiation leakage from the LINAC head occurs at the isocenter position.

1.1.4. Side effect of LINAC head leakage to patient

According to Kinsara et al. [23] research, the MCL in LINAC machine is one of the locations radiation leakage occurs and emits unwanted peripheral dose. Peripheral dose (out-of-field dose) means the dose beyond the radiation field's geometrical bounds during advanced cancer treatment techniques, such as external beam radiation therapy (EBRT), IMRT and VMAT. It can contribute to serious side effects and health risks for patients, including eye damage, sterility, and an increased risk of secondary cancer. Given the design of the LINAC machine and type of treatment, peripheral doses may account for 2–10% of the maximal dose delivered to the patient. For example, if a patient receives a total dose of 7000 cGy during cancer treatment, healthy organs may receive up to 665 cGy in total [23]. Therefore, many studies have investigated the side effects of out-of-field radiation, especially for secondary induced cancer. Kinsara et al. summarized the possible secondary cancers that can occur after radiation therapy, including breast, lung, bone sarcoma, soft tissue sarcoma, esophageal, stomach, colon, rectal, uterine corpus, bladder, and ovarian cancers. The health consequences of LINAC head leakage are mainly considered stochastic effects, meaning that the probability of secondary cancer induction increases with the received dose

[24]. Between radiation doses of 0.1 and 2 Sv, there is a linear relationship with secondary cancer induction. However, the dose-response relationship is still under discussion when doses are higher than 2 Sv. Kry et al. [25] summarized the neutron ambient dose equivalent ($H^*10(\mu Sv/MU)$) from out-of-field dose in different LINAC machines (Fig. 11). H^*10 is used to measure the biological effectiveness of neutron radiation, and $\mu Sv/MU$ represents the amount of neutron radiation produced by the LINAC per Monitor Unit (MU) of the primary X-ray beam. In a LINAC, 1 MU is typically calibrated to deliver 1 cGy of dose under reference conditions in a water phantom.

Neutron ambient dose equivalent (outside the treatment field)

Photon beams			Electron beams		
Linac	Energy	H*(10) (μSv/MU)	Linac	Energy	H*(10) (μSv/MU)
Varian	10	0.9	Varian	9	0.01
	15	9.4		12	0.04
	18	19		15–16	0.31
	20	26		18	1.6
Elekta	15	3.3		20	0.31
	18	8.4	Elekta	12	0.03
	22	37		15	0.54
Siemens	10	0.3	Siemens	15	0.05
	15	5.2		18	0.2
	18	5.6		21	0.25
	23	18			

Fig. 11. Summary of the neutron ambient dose equivalent induced by different LINAC machines (Kry et al., 2017)

Three types of LINAC machines included in the study: Varian, Elekta, and Siemens. Neutron ambient dose equivalent values were recorded beyond the treatment field, from 10 to 50 cm from central axis. All LINAC machines operated in both photon and electron modes at different energies, resulting in a neutron ambient dose equivalent from 0.01 to 37 $H^*10(\mu Sv/MU)$. Higher photon and electron beam energies resulted in greater neutron leakage. Therefore, unwanted neutron exposure outside the treatment field should be considered in radiation protection, as it may contribute to biological damage and increase the risk of secondary cancer induction [22].

1.2. Neutron shielding mechanism

A mixed radiation field including neutrons and high-energy photons are produced within the LINAC head during high-energy operation. Therefore, effective shielding materials should be used for attenuation both types of radiation. Also, neutrons interact strongly with materials through nuclear interactions, with the nature of the interaction depending heavily on their energy levels. Neutron energy is categorized into three main groups: thermal (~0.025 eV), intermediate (~0.025 eV to 100 keV), and fast neutrons (>100 keV, often up to several MeV) [49]. Effective neutron shielding involves two distinct steps: moderation and absorption. First, fast neutrons are slowed down by hydrogen-rich materials, and subsequently, the resulting thermal neutrons are captured by high cross-section materials.

Polyethylene is an effective material for neutron moderation due to its high hydrogen density and significant removal cross-section. As a polymer characterized by long chains of repeating ethylene (C_2H_4) units, it serves as an efficient moderator that thermalizes fast neutrons through elastic scattering. However, polyethylene is less effective for shielding thermal neutrons and high-energy photons because of its low thermal neutron capture cross-section and low atomic number. To address this limitation, it is frequently combined with materials having high thermal neutron absorption cross-sections and high-Z fillers, such as boron nitride, gadolinium(III) oxide, samarium(III) oxide, and bismuth- or tungsten-based fillers, to improve thermal neutron absorption and photon attenuation. These high thermal neutron cross-section and high-Z additives enhance the composite's protective capabilities against both thermal neutrons and secondary gamma radiation [7,26].

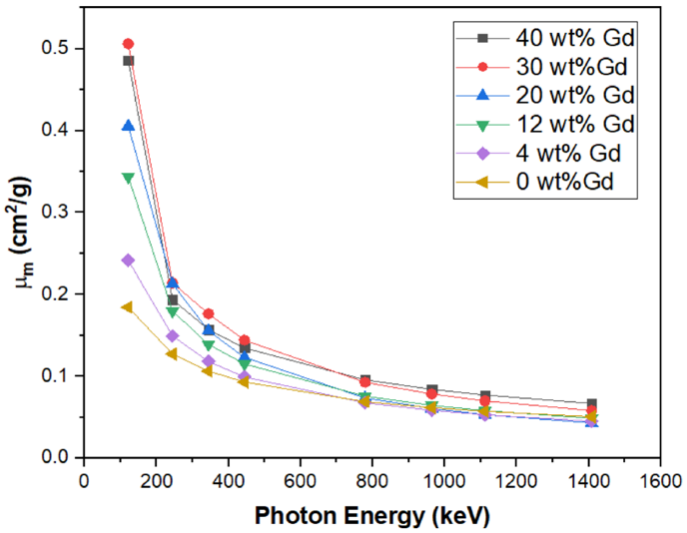

Fig. 12. Experimental mass attenuation coefficient results of HDPE reinforced with Gd_2O_3 fillers at different concentrations (M. Shabib et al., 2026)

The study by Mohamed et al. [7] investigated the neutron and gamma-ray shielding performance of HDPE/Gd_2O_3 composites. The experimental results demonstrated that the mass attenuation coefficient μ_m is enhanced with increasing Gd_2O_3 filler concentration at low-energy levels. At 121 keV, HDPE without fillers recorded a coefficient of 0.185 cm^2/g, while HDPE/40% Gd_2O_3 recorded the highest attenuation coefficients of 0.486 cm^2/g. At low photon energies (less than 779 keV), the photoelectric effect dominated, therefore, higher attenuation was measured due to Gd having a high atomic number. However, at high photon energies (larger than 779keV), Compton scattering dominated, which reduced the attenuation gradually.

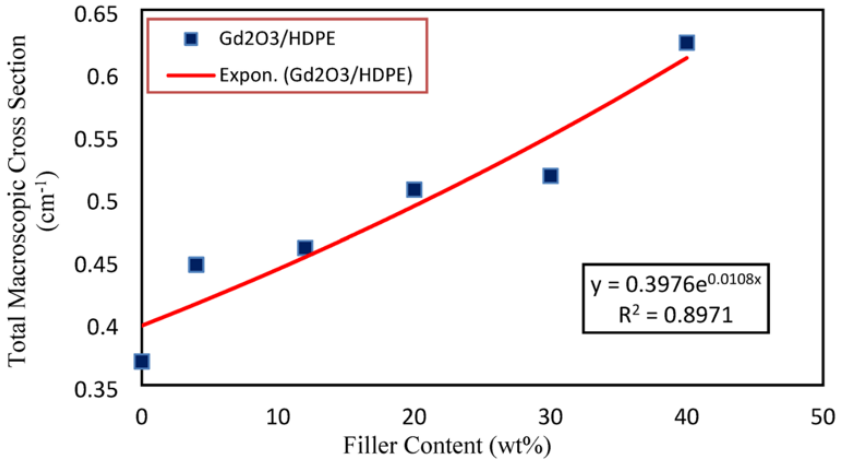

Fig. 13. The Gd2O3/HDPE composites' total macroscopic cross section value plot (M. Shabib et al., 2026)

Regarding neutron shielding performance, the results showed that Gd is a strong neutron absorber, as increasing the Gd_2O_3 content enhances the probability of thermal neutron interaction ($\sum_T$). The total macroscopic cross-section ($\sum_T$) is related to the probability of thermal neutron interaction, the higher the cross-section value, the better the neutron shielding performance. The results showed that the total macroscopic cross section increased from 0.369 cm^{-1} to 0.624 cm^{-1} as the Gd_2O_3 content rose from 0 wt% to 40 wt%. The relationship between $\sum_T$ and filler content obtained a 0.8971 R-squared value [7].

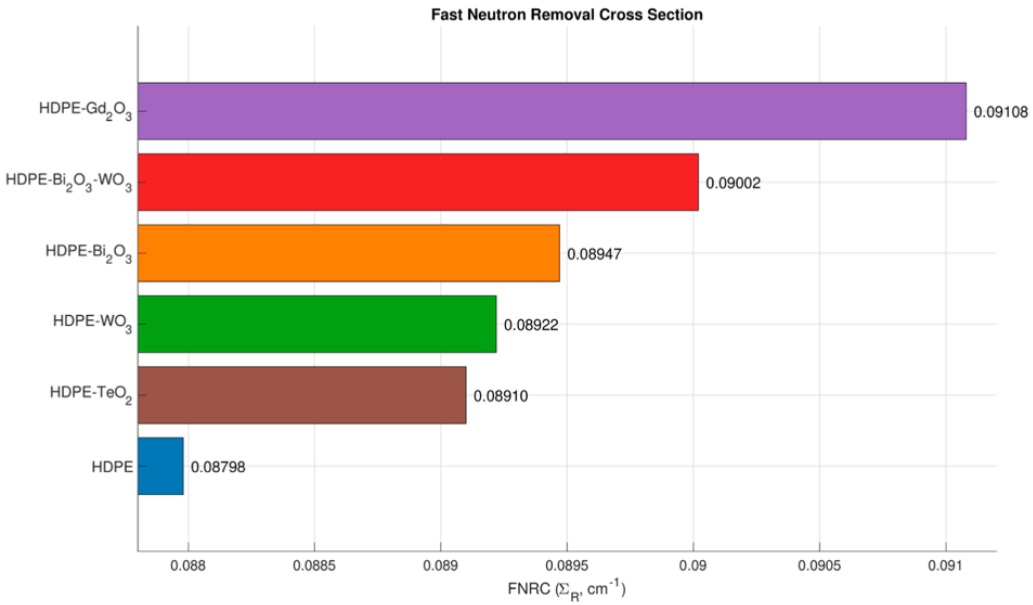

Fig. 14. Fast neutron removal cross section for HDPE/oxide composites (A. Alharbi et al., 2026)

On the other hand, A. Alharbi et al. studied the fast neutron and gamma ray (0.015-15 MeV) shielding performance of HDPE/high-z oxides composites. Simulations of HDPE composites reinforced with bismuth oxide, tungsten trioxide, gadolinium oxide, and tellurium dioxide at 60 wt% were evaluated. Phy-X/PSD with Geant4 Monte Carlo simulations obtained the fast removal cross section ($\sum_R$) value of these composites. The results showed that the

HDPE/Gd_2O_3 composites obtained the highest $\sum_R$ with 0.0911 cm^{-1}, followed by hybrid fillers (0.09 cm^{-1}), bismuth oxide (0.0895 cm^{-1}), tungsten trioxide (0.0892 cm^{-1}), and tellurium dioxide (0.0891 cm^{-1}). Gd_2O_3 had a superior neutron-capture potential, which enhanced the probability of interaction for thermal neutron attenuation. For gamma-ray shielding performance, tungsten trioxide and the hybrid fillers obtained the highest linear attenuation coefficients at low energies [27].

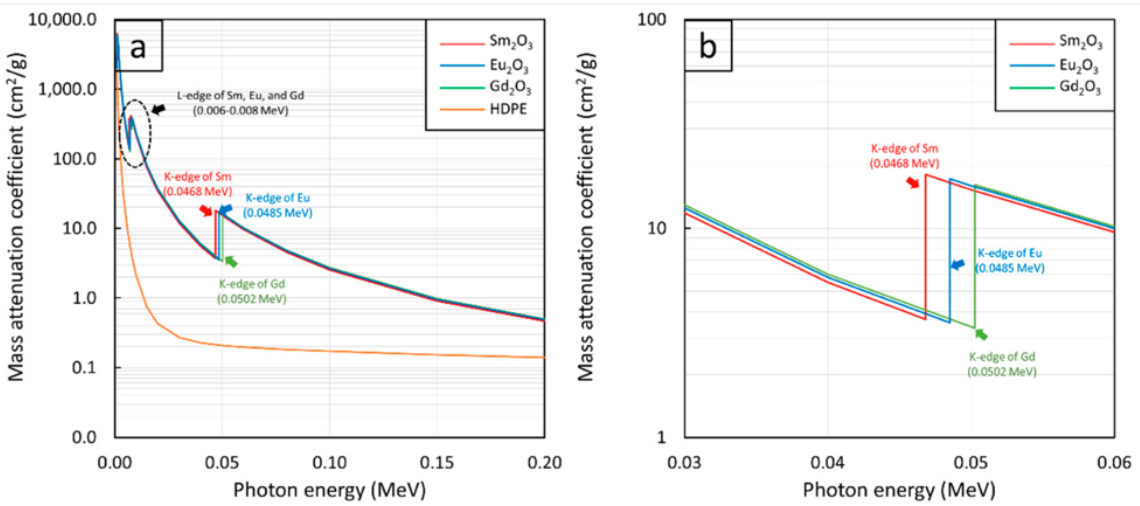

Fig. 15. Plots of mass attenuation coefficient against photon energy of rare-oxides/HDPE composites (K. Saenboonruang et al., 2021)

K. Saenboonruang et al. [28] also investigated the photon shielding performance of the HDPE composites reinforced with rare-earth oxides, including samarium oxide, gadolinium oxide, and europium oxide. PhyX/PSD and Monte Carlo transport simulations were carried out to find the linear attenuation coefficients and mass attenuation coefficients. The results showed that the linear attenuation coefficient increased with Gd_2O_3 filler concentration, where the 60 wt% Gd_2O_3 filler showed the highest enhancement compared to neat HDPE. Figure 15 indicates the K-edge and L-edge absorptions of different rare-oxide atoms, where the incident photon energy matches the binding energy of inner-shell electrons. The 'jump' represents the enhancement of the photon attenuation due to photoelectric effect. The L-edge occurs at around in 0.006-0.008 MeV, where the photons has just enough energy to eject electrons from the L-shells. The K-edge occurs in around 0.046-0.05 MeV, where incident photon energy overcomes the K-shell binding energy and knocks out an electron. The results indicated that Gd_2O_3 has the highest K-edge energy (0.0502 MeV) compared with Sm_2O_3 (0.0468 MeV) and Eu_2O_3 (0.0485 MeV). Therefore, Gd_2O_3 provides enhanced photon attenuation at slightly higher photon energies in this energy range [28].

All the studies indicated that the incorporation of Gd_2O_3 into HDPE composites significantly enhanced photon attenuation and the neutron shielding performance, particularly regarding the enhancement of the thermal neutron removal cross-section and mass attenuation coefficient.

1.3. Experimental setup

1.3.1. 3D Printing methods

3D printing is widely applied in the medical field. It is used to visualize human anatomy for surgical preparation, specialized medical procedure trainings, customized prosthetics and implants, doctor/patient education, and etc. Due to breakthroughs in advancing materials and printing techniques, 3D printing technology has developed rapidly and has become reliable and highly accurate. Different types of 3D printing technologies are applied in medical fields, and the cost of the machines varies depending on the printing technology, used materials, printing resolution, speed, software and etc [29].

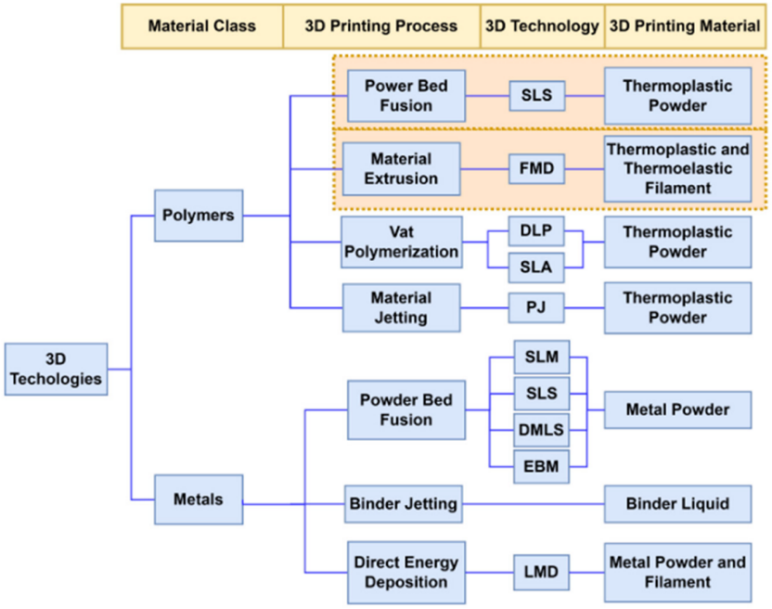

Fig. 16. 3D printing technologies classification (H. Alamei et al., 2022)

There are different technologies in 3D printing, including inkjet printing (IJP), fused filament (FFF), electron beam melting (EBM), fused deposition modeling (FDM), stereolithography (SLA), selective laser sintering (SLS), direct metal laser sintering (DMLS), PolyJet (PJET), and etc. To provide a clearer classification, the International Organization for Standardization (ISO) categorizes additive manufacturing (3D printing) technologies primarily by process type, while recognizing polymers and metals as the main material classes used within these processes. This report focuses on polymer materials, which involve four 3D printing processes, including power bed fusion, material extraction, vat polymerization and material jetting [30].

Power bed fusion uses a high-power laser or electron beam to fuse plastic or metal powder together. SLS 3D technology uses polymers, such as nylon, to build the models, which produce strong and functional parts and allow for complex geometries. The advantages of this technology are low cost, high productivity, stable performance, and the ability to print without using support structures [31].

Material extrusion is a technique where polymer materials are heated and extruded through the nozzle to form a model layer by layer. Usually, PLA, ABS, and PETG materials are used for this printing method, as they are easier and cheaper to print and provide strong mechanical resistant. FDM is the printing technology that is invented and patented by Stratasys. It is good for prototypes and building functional parts. However, it has lower resolution compared to other 3D printing technologies, and thermal management remains as a challenge. Degraded interlayer adhesion is caused when the printing speed increase, especially for ABS, which is sensitive to temperature change [32].

Vat polymerization is a technique that uses light to turn liquid resin into solid plastic. Examples include SLA and DLP. The vat container is filled with liquid photopolymer resin as the printing material, then by using a UV laser or projector, the resin hardened layer by layer. Along with the moving platform, these procedures repeat and form specific models. SLA technology photopolymerizes/hardens a liquid resin by using an ultraviolet laser, while DLP technology uses projector to cast light. The advantage of vat polymerization is its high resolution and precision, DLP achieves less than 100 μm resolution and models micron-scale features, which is perfect for printing biomedical scaffolds and microstructures. Also, it is fast in fabrication and offers thermal stability and good mechanical properties, which are provided by its cross-linked network with C-C backbone [33].

Material Jetting is 3D printing process that use droplets of liquid resin and UV light to cure them and to form a model. Usually, photopolymer resin is used and sprayed on the model surface, then instantly hardened using UV light. PJ is a 3D technology that is trademarked by Stratasys. The advantages of this technology are quick curing without concerns regarding evaporation or nozzle drying problems. However, this technology may not have been suitable for health and food industries due to the movement of hazardous materials [34].

1.3.2. Dosimetry

Photon detectors

There are various types of photon detectors available on the market. However, measuring the out-of-field dose remains as a significate challenge. There are four main challenges: (1) Misleading surface dose measurement. Since the stray electron enhances the surface dose by up to five times more than the deeper regions, a build-down effect occurs and overestimates the dose measured in the patient's body. (2) Radiation energy is softer out-of-field. The out-of-filed radiation energy (the lowest can be 0.2 MeV) is much lower than the treatment beam (1.5 MeV to 6 MV) itself, some of the detectors overrespond to the low-dose results, leading to an overestimation of the measured dose. (3) The out-of-field dose is low. As the dose is too low to show appropriate readings, it is common to increase the monitor unit (MU) during the phantom measurement, while this strategy cannot be applied to in vivo measurement. (4) The mixing of radiation field reduces the reliability of the measurement results. If there are mixed radiations such as, neutrons, protons, photons, electrons, the detector can respond differently in each measurement.

There are five main types of photon detectors, including TLD, OSLD, ion chamber, films, diodes, and MOSFETs. It is challenging to measure the accurate dose from different depths and angles, especially across various energy ranges, as most of the detectors are energy

dependent. Therefore, each type of the detector has its own advantages and disadvantages and is applied in different situations [25].

Table 1. Advantages and disadvantages of different type photon detector.

Photon detectors	Advantage	Disadvantage
Thermoluminescent Dosimeter (TLD), Optically Stimulated Luminescent Dosimeters (OSLD) [25,35]	Light weight, safe, used in vivo measurement	Overresponse to out-of-field dose measurement, such as TLD-100 (12% overresponse) and nanoDots (5%-31% overresponse)
Ion chamber [25]	Can be used for measuring nontarget dose, has good dose rate linearity and high accuracy, and can be used for a wide range of energy measurements	Bulky, energy highly dependent on the chamber material, sometimes overresponding to low dose, eg. Famer chamber and scanning chamber (5% overresponse), low readings may occur (requiring a longer collection time in low-charge situations)
Radiochromic films [25,36,37]	Used for quality assurance, "self-developing" and tissue-equivalent, accurate and reliable eg. XR, EBT films	EBT overresponse (8%), EBT2 & 3 overresponse (5-10%), dependent on orientation and kVp, needs calibration
Diodes [25,38]	Simple, low-cost, small field, used for in vivo measurement and quality assurance	Overresponse from high-Z materials, high-energy diodes were not accurate for out-of-fields measurement, SSD dependence (eg. EDD-5 diode), angular dependence
MOSFETs [25,38]	Used in vivo measurement, small size, instantaneous readout, simple to use, small field, energy independent (in MeV range of energy)	Need calibration, angular dependence, and temperature dependence (might need a correction factor)

Neutron detector

Neutron dosimetry is a challenging topic, as neutron act differently than photons, and the detectors highly depend on the neutron energies. First, neutron detectors are only sensitive to a specific energy range, meaning the neutrons collected by the detector cannot reflect the actual amount of neutrons delivered. This can make the results vary from the actual neutron quantity. Second, the energy spectrum of neutrons changes through scattering in patient or phantom. Neutron detectors are usually operated in air to obtain accurate dose and neutron spectrum measurements; however, the dose equivalent in air does not represent the actual dose received by patients. Summarizing the above factors, it is important to understand the neutron detector sensitivity to energy spectrum and use corrections rather than relying only on air-based calibration [25].

Thermal neutron detector

Thermal neutron detectors can be classified into two types: active and passive. Active detectors show the dose in real time, while passive detectors integrate the dose over time.

For thermal active neutron detectors, helium-3 (^{3}He) or boron-10 (^{10}B) are commonly used as the detection material because both have very high thermal neutron absorption cross sections, allowing efficient detection through nuclear reactions [39,40,41]. As neutrons cannot be detected directly, they need to be captured and converted into charged particles through a nuclear reaction before detection. In a boron gas neutron detector, the ^{10}B(n,a) reaction is conducted, also called as a capture reaction, where the neutron is captured by the boron gas, which then emitted alpha radiation. An example is shown in equation 3 [39]:

$$^{10}_{5}B + \ ^{1}_{0}n \rightarrow \ ^{7}_{3}Li + ^{4}_{2}He \quad (3)$$

The study by Z. Uddin, et al. [42] used a ^{3}He neutron dosimeter to investigate the neutron shielding properties of polyethylene with boron carbide composites. They used an Am-Be neutron source with 4.5 MeV, which matched the ^{3}He neutron dosimeter's sensitive energy range (~4.5-5 MeV) [43].

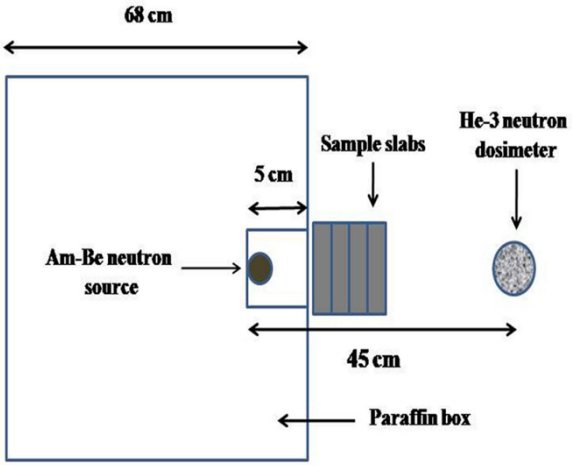

Fig 17. Experimental setup for investigating neutron shielding properties (Z. Uddin et al., 2020)

For thermal passive neutron detectors, two main types are commonly used: activation foils and thermoluminescent dosimeters (TLDs). According to IAEA safety guidelines, TLDs are often enriched with ^{6}Li or ^{10}B to detect neutrons, using materials such as LiF and $Li_2B_4O_7$. TLDs are typically used in pairs: (1) TLD-600, enriched with ^{6}Li, which is sensitive to both neutrons and photons, and (2) TLD-700, enriched with ^{7}Li, which is sensitive only to photons [44].

Additionally, activation foils are thin metal discs made of materials such as gold (^{197}Au) or indium (^{115}In). When these foils capture thermal neutrons, they become radioactive and subsequently emit gamma radiation. The intensity of the emitted gamma rays is then measured to determine the corresponding neutron flux. An example is shown in equation 4:

$$^{197}_{79}Au + ^{1}_{0}n \rightarrow ^{198}_{79}Au + \gamma\ (411\ KeV) \quad (4)$$

However, in many practical situations, such as radiation shielding, nuclear reactors, and radiation therapy, fast neutrons can make a significant contribution to the dose. Therefore, it is important to use the thermal neutron detector–moderator systems to determine the data related to fast neutrons. This means the neutrons have to pass through a moderator first, in order to be slowed down before being detected by the thermal neutron detector [25]. The Bonner sphere spectrometer is one example of this approach, where polyethylene spheres of different diameters, usually about 6–12 spheres, are placed around a thermal neutron detector. Each sphere slows down neutrons to a different degree because of differences in sphere thickness. Therefore, the neutron energy spectrum can be estimated by comparing and analyzing the results obtained from all spheres [45].

Fast neutron detector

For the fast neutron detector, the bubble detector is one of the examples [25]. The bubble detector is a small, sealed tube filled with a gel-like elastic polymer and droplets of superheated liquid. It has a neutron detecting energy range of around 100 keV-20 MeV with an accuracy of ± 20%. The working principle is that when a neutron is captured by the detector, it produces secondary charged particles, and the energy is deposited in the droplet to form a bubble. Therefore, a real time (active) result can be recorded by this bubble detector [46].

Fig. 18. The bubble detector (E. Ramalho et al., 2011)

Based on the reviewed literature, previous studies have highlighted both the sources and mechanisms of radiation leakage in LINAC head, as well as the limitations of conventional shielding materials. Literature review has shown that leakage radiation is mainly composed of neutrons and high-energy photons, which requires shielding materials capable of handling both radiations effectively.

The aim of this work is: To investigate the suitability and effectiveness of Gd3O2 reinforced HDPE composite materials as potential shielding solutions for mixed neutron and high-energy photon radiation environments encountered in LINAC machine.

Following tasks are set to implement the aim:

1. Fabricate HDPE/Gd_2O_3 composite filaments with controlled Gd_2O_3 weight fractions to achieve suitable printability.
2. Print samples from the produced filaments in geometries designed for mechanical testing and radiation attenuation measurements.
3. Characterize the mechanical properties of the composites and determine whether the materials possess sufficient mechanical strength and durability for potential shielding applications.
4. Evaluate the radiation attenuation performance of fabricated composites in mixed neutron–photon fields by using dosimetric film measurements.
5. To assess whether the composites provide improved shielding performance compared with pure HDPE.

2. Materials and methods

2.1. Filament production

In this report, three different types of filaments were produced by using an 3Devo extruder, including pure HDPE, HDPE/5 wt% Gd_2O_3, and HDPE/10 wt% Gd_2O_3 were fabricated by the extruder. The filament diameter was maintained at a target of 1.75 mm ± 0.05 mm. Variations outside 5 mm, as deviations beyond this range impacted the tolerance significantly compromised the stability of the subsequent 3D printing process. Specifically, diameters below 1.70 mm resulted in under-extrusion and reduced specimen density, whereas diameters exceeding 1.80 mm led to mechanical occlusion within the extrusion path. To ensure consistency, the filament diameter was monitored and verified through micrometer.

The characteristics of HDPE granules and Gd_2O_3 powder are shown in Table 2. The geometry of Gd_2O_3 is shown in Figure 19, where the Gd-O distance was 2.81 Å, the Gd-Gd distance was 2.11 Å, and the O-O distance was 2.74 Å [47].

Table 2. Characteristics of HDPE granules and Gd_2O_3 powder

Composites	Theoretical Density (g/cm^3)	Melting point	Formula
HDPE	0.95	120-130°C	$(C_2H_4)_n$
Gd_2O_3	7.40	2330 - 2350°C	Gd_2O_3

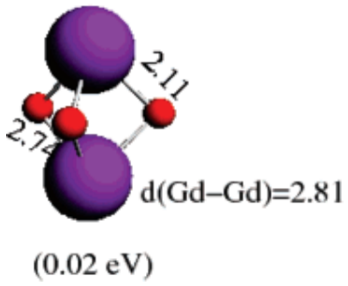

Fig. 19. The Gd2O3 geometry (A. Ayuela et al., 2007)

Fig. 20. 3Devo filament extruder

The filament in this report was fabricated by using 3Devo Precision (3Devo, Utrecht, Netherlands) filament extruder. The apparatus comprised four main parts, including the heaters, the extruder head, the puller, and the colling system. The heaters maintained thermal control to melt the granules, ensuring a consistent flow through the nozzle. The colling system facilitated thermal stabilization, while the puller provided the tension to form the filament shape in a suitable diameter. Thermal regulation was a critical parameter in filament production. The 3Devo system employed four heating systems labeled as H1, H2, H3, and H4 in Fig. 21. Initially, material was fed into the hopper and moved by a screw. The feeding process was governed by the H4 and H3 melting the granules. Following this, in the transitioning process, H3 and H2 compressed the granules to reach a fully melted state. Finally, the metering process was regulated by H1 to control filament formation and texture. Therefore, the temperature of the heaters, extruder speed, and fans speed were calibrated carefully based on these functions and principles, as detailed in the methods section.

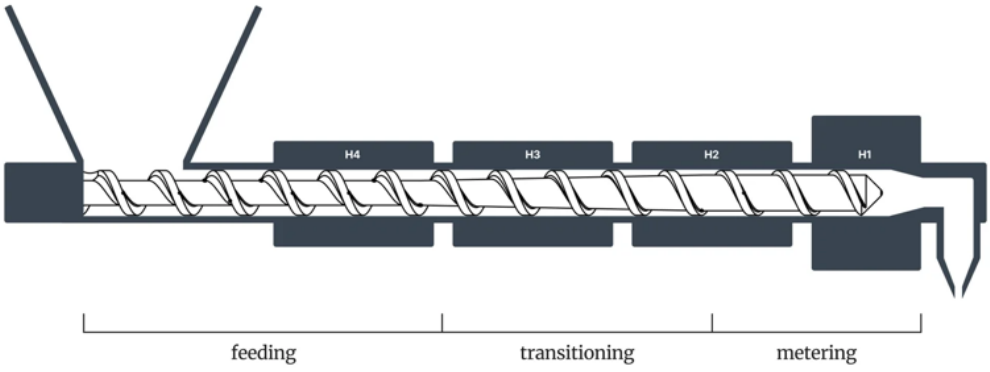

Fig. 21. Heater zones in the extruder

Before filament production, it was important to clean the extruder to avoid contamination or mixing with previously processed materials. 3Devo recommended using purging materials, including DevoClean MidTemp (200-300°C), DevoClean HighTemp (290-400°C), and 3Devo HDPE (180-280°C). The standard cleaning was performed using DevoClean MidTemp, then gradually reduced and replaced with 3Devo HDPE. If a heavy purge was needed, DevoClean HighTemp was used, followed by a gradual reduction in temperature and replacement with DevoClean MidTemp then 3Devo HDPE. Before cleaning, the

ventilation was turned on, and cardboard was used to cover the sensors. All procedures were carried out according to the instructions provided on the 3Devo website.

For HDPE filament production, HDPE granules were put in the extruder. After the granules were melted by the heaters, the filament was extruded through the nozzle. It was important to turn off the fans during the whole process and maintain the consistent temperature. As HDPE was sensitive to temperature variation, which influenced its viscosity and melt flow behavior, fluctuations led to dimensional inaccuracies and poor adhesion, therefore, precise temperature control was essential for stable processing.

For the production of HDPE/5%Gd_2O_3 and HDPE/10%Gd_2O_3 filament, the two materials were first mixed together using castor oil as a binding agent. Castor oil facilitated the uniform adhesion of Gd_2O_3 powder to the surface of the HDPE granules. While no specific standard was established for the quantity of castor oil required, the volume was optimized to ensure complete surface coverage of the granules. Two other methods were evaluated but proved unsuccessful in achieving precursor uniformity, including mechanical grinding and melt-blending methods.

Fig. 22. Castor oil (left), mixed material (middle), mixed material in extruder (right)

Then, the mixture was processed through the extruder using the parameters specified in Table 2. During the filament production process, the heater temperature and the extruder speed required periodic recalibration due to inherent variations in system performance. These fluctuations were because of the mechanical behavior and environmental ambient conditions, which affected how the filament melted and flowed. Therefore, continuous monitoring and manual adjustment of these parameters were important to ensure dimensional stability and consistent filament quality throughout the extrusion process.

2.2. 3D printing

In this report, all the samples (HDPE, HDPE/5%Gd_2O_3, and HDPE/10% Gd_2O_3) and ISO 527-2 type 1BA test specimens were printed using a Creality K2 Plus 3D printer (Shenzhen Creality 3D Technology, Shenzhen, Guangdong, China).

The 3D printer used in this study has overall dimensions of 495 × 515 × 640 mm and a maximum printable volume of 350 × 350 × 350 mm. The nozzle diameter used in this report is 0.4mm with an extrusion temperature of up to approximately 250°C. The printer is equipped with a print-bed capable of reaching temperatures up to 120 °C, while the enclosed

chamber temperature can be elevated to 60 °C. The 3D printer supports different filaments, including PETG, PLA, PLA-CF, PET, ABS, ASA, and PPA-CF. Filament feeding can be performed through CFS or PTFE; however, only the PTFE tube was used in this experiment. All printing parameters can be manually set through the touchscreen, such as nozzle temperature, hotbed temperature, fan speed.

The Creality K2 Plus 3D printer utilized the FMD layer-by-layer printing method within the material extrusion technique. Throughout the experimental process, several technical challenges were encountered, including thermal management, printing accuracy, and the control of infill density, infill patterns, and printing speed. Additionally, the choice of material influenced the printer parameter settings, as HDPE, a high-shrinkage material, is highly sensitive to temperature changes, resulting in a greater risk of warping and interlayer defects [32].

Fig. 23. Creality K2 Plus 3D printer (left), and the printing process (right)

It was important to balance all parameters and impacts to print high-quality samples. Therefore, this report listed the main parameter settings, the production process, and the results of various trials. The parameter settings for the samples and Iso527 type 1BA bone shapes are provided in the result section.

The software used to control the parameters was Crealitycloud (Shenzhen Creality 3D Technology, Shenzhen, Guangdong, China), which is available as a web-based and mobile application. The software provides a massive 3D model library where user can access millions of 3D models and use the slicing function to adjust them. At the same time, users can download STL files, upload their own designs, and sell their creative models online. Crealitycloud featured a cloud slicing function that can convert STL files to G-code directly in cloud (via website, mobile device, or tablet). Users can adjust and control all parameters, such asl layer height, print speed, fan speed, and infill density. After setting the parameters, remote printing and monitoring are applied, allowing the user to control the printer from anywhere in real time. Lastly, users can share the results (model design and printing parameters) on the platform for free access. All information is available on Crealitycloud website.

2.2.1. Sample and test specimens design

Creality Cloud was used to prepare and slice a cylindrical sample with a diameter of 20 mm and a thickness of 5 mm with 100% infill (Fig. 26), as well as the test specimens - ISO 527-2 type 1BA (Fig. 24).

To perform a tensile test, test specimens had to be prepared to evaluate mechanical properties. The ISO 527 type was specifically used to determinate the tensile properties of plastics fabricated in standardized geometries, shapes, and dimensions (Fig. 25). Type 1BA had a reduction factor of 1:2 compared to the 1B for use with limited quantities of materials. The British Standard Institution (BSI) provided the standard dimension for the test specimens which were accredited as European Standard and approved by CEN [48]. In this report, HDPE, HDPE/5%Gd_2O_3 and HDPE/10%Gd_2O_3 test specimens were produced. Each type of materials had five specimens: two before irradiation, and three after irradiation.

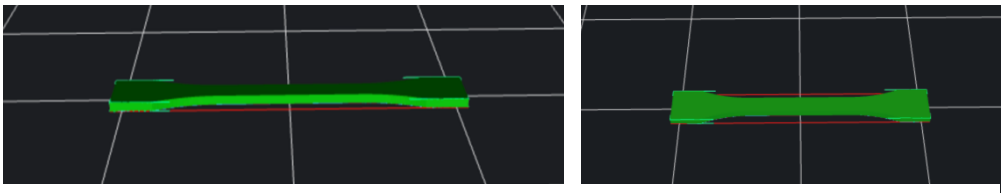

Fig. 24. Modelling of test specimen in ISO 527-2 Type 1BA

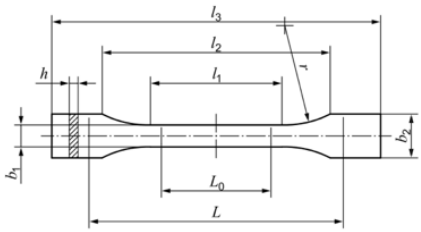

Figure A.1 — Type 1BA and 1BB test specimens

Table A.1 — Dimensions of type 1BA and 1BB test specimens

Dimensions in millimetres

	Specimen type	1BA	1BB
l_3	Overall length	≥75	≥30
l_1	Length of narrow parallel-sided portion	30,0 ± 0,5	12,0 ± 0,5
r	Radius	≥30	≥12
l_2	Distance between broad parallel-sided portions	58 ± 2	23 ± 2
b_2	Width at ends	10,0 ± 0,5	4 ± 02
b_1	Width at narrow portion	5,0 ± 0,5	2,0 ± 0,2
h	Thickness	≥2	≥2
L_0	Gauge length	25,0 ± 0,5	10,0 ± 0,2
L	Initial distance between grips	$l_2{}^{+2}_{0}$	$l_2{}^{+1}_{0}$

NOTE The specimen types 1BA and 1BB are proportionally scaled to type 1B with a reduction factor of 1:2 and 1:5, respectively, with the exception of thickness.

Fig. 25. Standard tensile test specimen of ISO 527-2 Type 1BA and 1BB (BSI, 2012)

The cylindrical sample model, with a diameter of 20 mm and a thickness of 5 mm, was designed for testing radiation shielding performance. The advantages of using a cylinder model included its smooth geometry without corners, as sharp corners enhanced the warping issues during 3D printing. In this report, samples of three materials were fabricated: HDPE, HDPE/5% Gd_2O_3 and HDPE/10% Gd_2O_3.

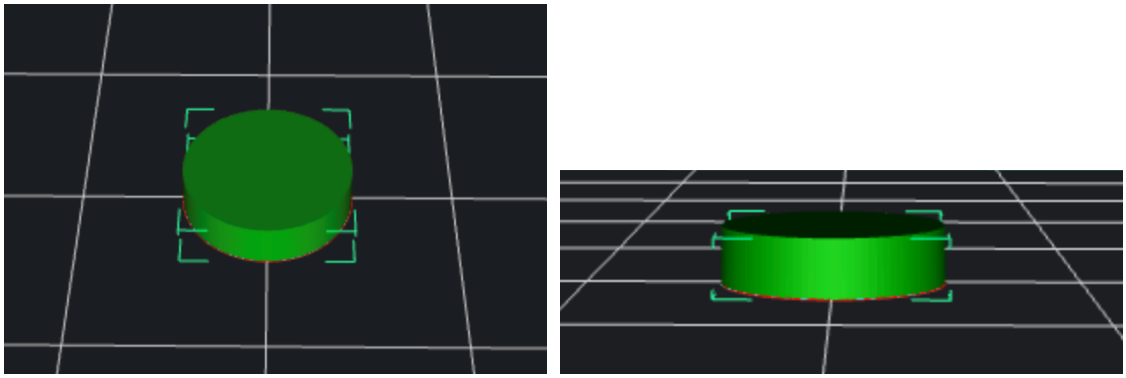

Fig. 26. Modelling of sample

There were two main adjustable parameters of 3D printing: 'filament' and 'process'. These controlled how the material was extruded and how the model was formed. Filament parameters describe the material properties by controlling melt and flow behavior, defining temperature requirements, and adjusting extrusion characteristics such as nozzle temperature, bed temperature, flow rate, and material density. In contrast, process parameters define how the model is printed by regulating cooling and printing conditions that influence geometry formation, surface quality, and mechanical strength. These parameters include layer height, print speed, infill density, and wall thickness. The suggested printing parameters for HDPE, and HDPE reinforced with Gd_2O_3 materials are indicated in the result section.

After the fabrication of the sample, weight was measured by using a digital weighting balance with maximum capacity of 210 g and readability of 0.1 mg. The measured weight was used for density calculations and compared to the theoretical density using the following equations (5,6):

The experimental density calculation:

$$\rho = m/V, \tag{5}$$

where m is the mass of the sample and V is the volume of the sample

The theoretical density of mixed material calculation:

$$\frac{1}{p_{th}} = \frac{w_x}{p_x} + \frac{w_y}{p_y}, \tag{6}$$

where p_{th} represented the theoretical density of mixed material;

w_x and w_y represented the weight fraction of the composited;

p_x and p_y represented the density of the material

The density percentage different calculation:

$$Precentage\ Different = \frac{|Expermental - Theoretical|}{Theoretical} \tag{7}$$

2.2.2. Magigoo PP glue application

Magigoo PP is a glue designed for polypropylene filament, which helps the prints stick to the print-bed. Since HDPE-based composites have poor adhesion issues, a thin layer of glue was applied and spread evenly before heating the print-bed. PP glue was used for HDPE because both are polyolefin polymers with similar molecular structures. This improves adhesion between the material and the print bed. The glue also helped reduce warping caused by HDPE shrinkage during cooling. It should be noted that the adhesive was corrosive and could cause eyes damage, therefore, it was important to be careful while using it.

Fig. 27. Glue (left), illustration of using the glue (right)

Once the printed sample was cooled down, it was gently peeled away from the brim or carefully removed using a scraper. To remove the adhesive, warm water and sponge were used to scrabe off the residue, and the print bed was dried with towel afterward.

2.3. Mechanical test

2.3.1. Tensile test methodology

A universal testing machine (UTM) Tinius Olsen H25 KT (Tinius Olsen, Horsham, United States), equipped with 25 kN load cell, was used to measure the tensile specimen strength. The specimens were tested at loading speeds of 20 mm/min. The measured properties included tensile strength, modulus, yield strain, and nominal strain at break.

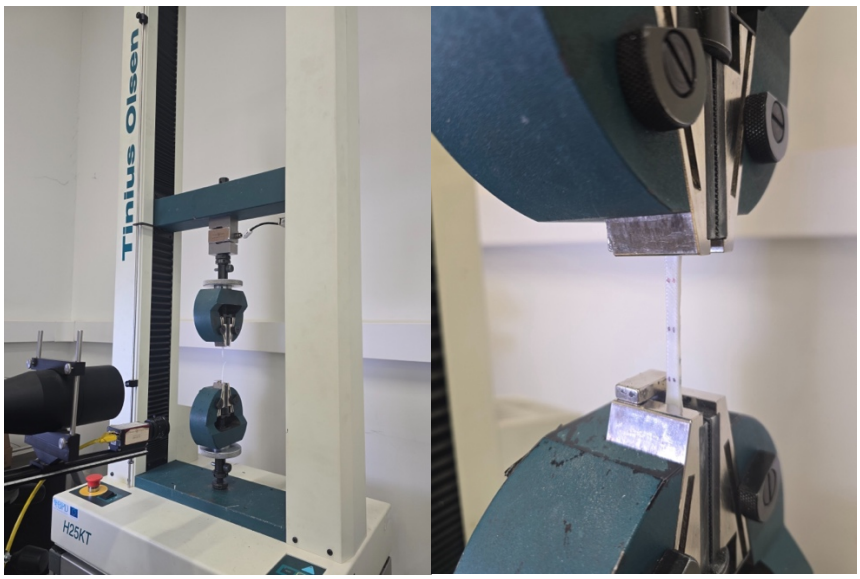

Fig. 28. Universal testing machine Tinius Olsen H25 KT machine(left), and the tensile test process(right)

2.3.2. Theoretical calculations of attenuation properties

The Neutron-Gamma Simulation software (NGCal) was used to evaluate the radiation shielding properties by calculating the theoretical mass attenuation factor (cm^2/g) for thermal and fast neutrons. It provided the attenuation simulations of thermal neutrons (25.4 meV) by using absorption cross-section data and fast neutrons (4 MeV) by using the removal cross-section value(Σ_R).

Additionally, the Phy-X/PSD software was used to evaluate the neutron shielding performance of the developed materials by calculating the theoretical fast neutron removal cross sections (FNRCS) (cm^{-1}) for fast neutrons (4MeV).

Furthermore, the XCOM simulation program was utilized to calculate the theoretical mass attenuation coefficients (MAC) (cm^2/g) for photons over a selected energy range.

The calculation of both neutron and photon attenuation properties are important because shielding materials are exposed to mixed radiation fields containing neutrons and high-energy photons simultaneously.

Formulars and weight fractions were used as input parameters in NGCal, Phy-X/PSD, and XCOM simulations to calculate the theoretical mass attenuation factor, FNRCS and MAC, respectively, as shown in Table 3.

Table 3. HDPE-based composites' formula by weight

Composites	Chemical formulas
HDPE	C_2H_4
HDPE/5% Gd_2O_3	0.95 wt%C_2H_4 + 0.05 wt% Gd_2O_3
HDPE/10% Gd_2O_3	0.9 wt% C_2H_4 + 0.1 wt% Gd_2O_3

2.3.3. Experimental setup of attenuation test

Neutron Source

In this report, radiation attenuation measurements were performed using a neutron source at the Center for Physical Sciences and Technology, Department of Nuclear Research. This approach was selected because the absence of a well-defined narrow neutron beam from the LINAC head limits its applicability for experimental attenuation studies. Therefore, a directional mixed radiation neutron source was selected to obtain more reliable measurements. Furthermore, the Pu–Be neutron source used in this report produces neutrons with energies higher than typical photoneutrons generated in a LINAC head. Therefore, if the developed shielding material can effectively attenuate higher-energy Pu–Be neutrons, it may also show promising shielding performance for LINAC photoneutron applications.

The samples were irradiated using a mixed radiation field produced by plutonium-based sources. The irradiation setup consisted of four separate sources housed in individual glass containers: two ^{238}Pu–Be neutron sources, one ^{239}Pu–Be neutron source, and one ^{238}Pu source.

Fig. 29. Shielded concrete construction with the central irradiation channel (left) and holder container with samples (right)

The schematic of the structure, shown in Figures 29 and 30, indicates that the samples, together with Gafchromic™ EBT3 films, were placed above the neutron sources for irradiation along the central channel. The neutron source container was surrounded by paraffin and concrete shielding, while beryllium was included as part of the neutron source/moderating assembly.

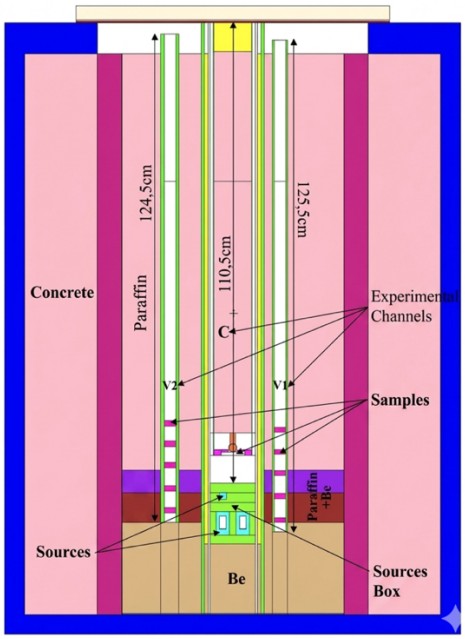

Fig. 30. Schematic of the structure of neutron sources

For this study, the irradiation was conducted via the central channel (without a cover), which provided a total neutron flux of 6.85×10^4 n/cm^2/s and a dose rate of 30 mSv/h. The neutron energy spectrum within this channel consisted of 65% thermal, 9% of epithermal and 26% of fast neutrons. The neutron energy spectrum of central channel is shown in Figure 31. there is a sharp flux peak representing thermal neutron energy.

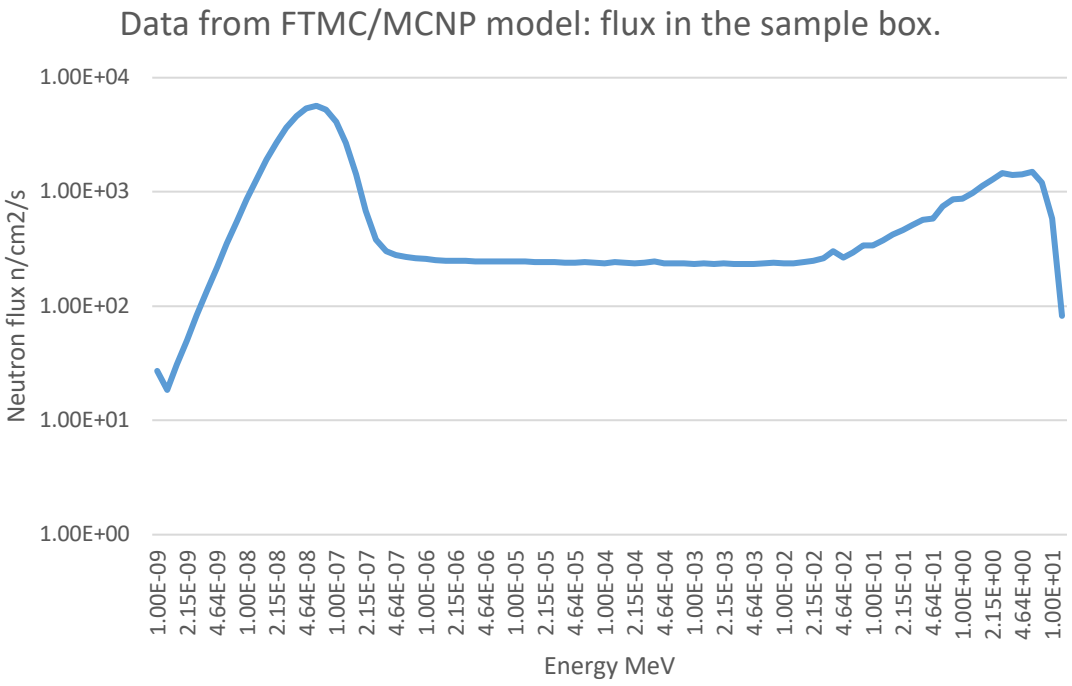

Fig. 31. Neutron spectrum of central channel

Dosimetry

In this report, GafchromicTM EBT3 films (Ashland Advanced Materials, Bridgewater, NJ, USA) were utilized to quantify radiation attenuation within the fabricated materials. Radiochromic film dosimeters exhibit a coloration change upon exposure to ionizing radiation. The EBT3 films were prepared in 20x20 mm square dimensions and were subjected to irradiation from the neutron sources. Calibration curve, correlating optical density with absorbed dose, were established by determining the mean pixel value of the non-irradiated films. These films were digitized using a photo scanner HP Scanjet G4050 (Hewlett-Packard, Palo Alto, CA, USA) (Figure 32) at a resolution of 600 DPI in TIF format and processed using the red channel with ImageJ software, version 1.54g (National Institutes of Health, Bethesda, MD, USA).

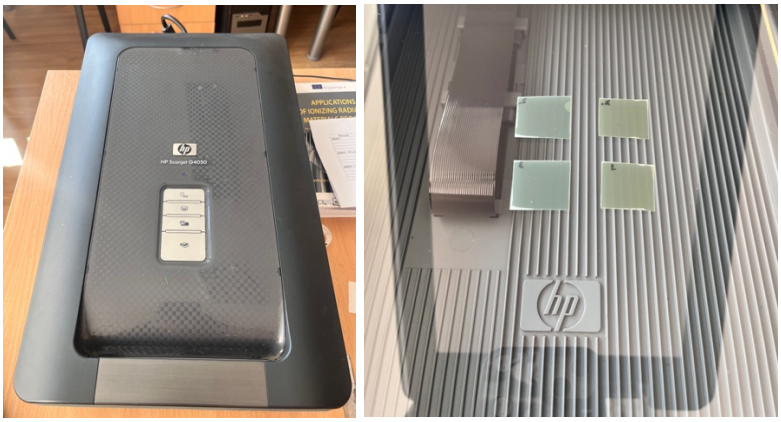

Fig. 32. HP Scanjet G4050 machine for scanning (left), and the process of film scanning (right)

The determination of radiation dose was performed using Gafchromic EBT3 film dosimetry, a process initiated by establishing a calibration curve that correlates the net optical density of the film to known absorbed doses. The net optical density was calculated using the ratio of pixel intensities from unexposed and exposed film scans, as shown in equation 8. Once the calibration function was defined, the measured dose for each experimental setup was determined by applying the film's optical response to the curve.

$$OD = log_{10}\left(\frac{P_0}{P}\right), \tag{8}$$

which P_0 represented the incident light intensity, and P represented the transmitted light intensity. To evaluate the shielding performance of HDPE/Gd_2O_3 composites, transmission and attenuation percentage values are calculated using equation 9 and 10, respectively.

$$Transmission\ (I) = \frac{D}{D_0}, \tag{9}$$

where D and D_0 represented the measured dose and incident dose respectively.

$$Attenuation\ percentage = \left(1 - \frac{D}{D_0}\right) * 100 \tag{10}$$

In the results section, the attenuation of the HDPE/Gd_2O_3 composite samples are comparatively analyzed.

3. Result and discussion

3.1. Filament production

Three different filaments were produced: HDPE, HDPE/5%Gd_2O_3, and HDPE/10%Gd_2O_3 which shown in figure 33.

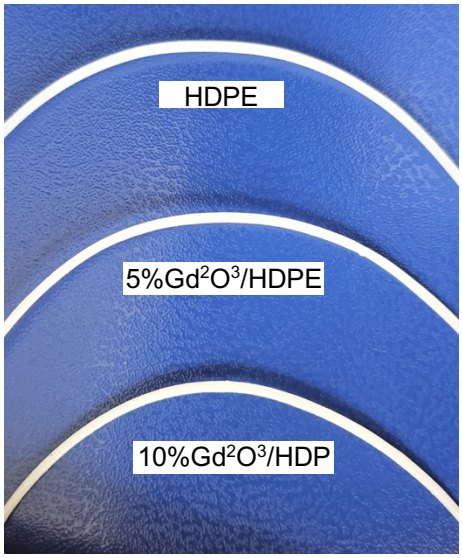

Fig. 33. Filaments produced from the prepared composite materials.

The characteristics of the filaments differed according to the material composition. Pure HDPE filament exhibited greater transparency, smoother surface and higher flexibility compared to filaments incorporated with Gd_2O_3 fillers. While HDPE with 5% and 10% Gd_2O_3-filled composites filament demonstrated relatively higher stiffness, slightly textured surface, and lower transparency. On the other hand, all the extruded filaments' diameters were within acceptable value of tolerance ± 0.05 mm.

Table 4. Extruded filaments' characteristics

Material	Filament diameter(mm)	Characteristics
HDPE	1.75 ± 0.03	Smooth surface, higher flexibility, more transparency
HDPE/5%Gd_2O_3	1.75 ± 0.04	Slightly textured surface, less flexibility, less transparency
HDPE/10%Gd_2O_3	1.75 ± 0.05	Slightly textured surface, less flexibility, less transparency

The reduction of flexibility and surface smoothness might have a detrimental effect on the 3D printing samples. During FDM, feeding and deposition required sufficient flexibility of filament. Also, the textured filament at higher Gd_2O_3 concentrations might increase the viscosity and affect the interlayer adhesion during 3D printing process.

During the filament extruding process, the operating parameters were systematically adjusted according to the heater temperatures, extruder speed (rmp), and cooling fans speed to ensure stable processing conditions.

Table 5. Extruder's parameters in filament production

Parameters/Filaments	**HDPE**	**HDPE/5%Gd_2O_3 & HDPE/10%Gd_2O_3**
Heater 1(°C)	186 - 190	188 -212
Heater 2(°C)	195 - 220	200 - 222
Heater 3(°C)	203 - 205	206 - 229
Heater 4(°C)	203 - 205	206 - 209
Extruder speed (rpm)	2.5	1.8 - 1.9
Fans speed	0	0

The temperatures of heaters were carefully controlled during the extrusion process. As shown in Table 5, the H4 and H3 were set higher than those of H2 and H1 to enable effective melting of the polymer granules. In order to maintain dimensional stability and guarantee a smooth surface, a gradual reduction in temperature was implemented in H2 and H1 to avoid excessive melt fluidity.

During the filament production, the extruder speed (rpm) played an important role in regulating the internal pressure and flow rate. The results showed that pure HDPE filament required a higher extruder speed compared to HDPE/5 Gd_2O_3 and HDPE/ Gd_2O_3 composites. This observation suggests that the incorporation of Gd_2O_3 fillers influences the melt behavior of polymer matrix. The presence of Gd_2O_3 may have contributed to improved the thermal stability and reduced material deformation during the extrusion process, resulting in more stable filament formation.

Additionally, maintaining heater temperatures at the lowest effective range is crucial, as too high thermal exposure may result in polymer deterioration. Furthermore, because HDPE and incorporation of Gd_2O_3 fillers filaments were extremely sensitive to temperature changes, cooling fans were found to be inappropriate for its manufacture. Immediate cooling caused early solidification, which degraded the surface quality and uniformity of the filament.

Fig. 34. Spooling of HDPE filament

The spooling process was performed to ensure proper filament handling, maintain dimensional stability, and prevent deformation or tangling during storage. Proper spooling also helped preserve the mechanical integrity and uniform geometry of the extruded filaments, which are important for achieving stable and consistent printing performance. All fabricated filaments were subsequently collected onto a printer spool at a collection rate ranging from approximately 4.50 to 6.25 mm/s, depending on the screw speed, which varied between 1.8 and 2.5 rpm.

3.2. 3D printed result of samples and test specimen

To achieve consistent filament extrusion and high-quality 3D printed samples, appropriate printing parameters were established through experimental investigation. The selected conditions demonstrated effective printing performance and satisfactory print quality throughout the fabrication process.

For the 3D printing setting, '0.20mm standard@K2 Plus' profile with moderated parameters configurations was applied. The printing parameters considered five main aspects: quality, strength, speed, support, and auxiliary settings. In the filament settings, CR-HDPE material was selected with moderate parameter adjustments. The recommended printing parameters used in this study are presented in Table 6.

Table 6. 3D printing parameters in different materials

Filament Parameters/Materials	**HDPE**	**HDPE/5%Gd_2O_3 and HDPE/10%Gd_2O_3**
Shrinkage xy	99%	98%
Nozzle temperature	Min: 220°C; Max 235°C	Min: 216°C; Max: 220°C
Printer chamber temperature	35°C	35°C
Print temperature	First layer: 230°C; Other layers: 230°C	First layer: 220°C; Other layers: 216°C
Bed temperature (Smooth PEL Plate)	First layer: 110°C; Other layers: 100°C	First layer: 110°C; Other layers: 106°C
First layer printing speed	15 mm/s	23 mm/s
Other layer printing speed	Inner wall: 25 mm/s Outer wall: 20 mm/s	Inner wall: 30 mm/s Outer wall: 38 mm/s
Top/bottom surface pattern	Monotonic line	Monotonic line
Infill layer pattern	Line	Line
Space infill density	100%	100%
Brim type	Outer and inner brim	Outer and inner brim
Brim width	20mm	20mm

The HDPE filament filled with Gd_2O_3 fillers significantly affected the thermal and rheological behavior of the material, which required different 3D printing settings. The extruded filament solidified relatively faster upon deposition, allowing lower nozzle and bed temperatures compared to pure HDPE filament. Additionally, the Gd_2O_3 fillers caused the polymer melt to become more viscous, resulting surface imperfections in the filament, which enhanced the resistance during extrusion. A relatively faster printing speed was needed to compensate for this decreased flowability and ensure a smooth deposition process. This was expected as HDPE material has a massive shrinkage and adhesion issues, while the addition of fillers can overcome the warping, blending and deformation problem, resulting an improvement of stable printability [50,51].

During the printing process, the fan speeds were adjusted in real time depending on the observed performance of the printed samples and test specimens (Table 7). This included both the side cooling fans and the case fans. Such adjustments were important to regulate the cooling rate of the extruded material, to optimizing solidification and maintaining interlayer adhesion with high quality printing.

Table 7. Fans speed setting for 3D printing

Fans parameters/Materials		**HDPE**		**HDPE/5%Gd_2O_3**		**HDPE/10%Gd_2O_3**	
		Sample	Test specimens	Sample	Test specimens	Sample	Test specimens
Case fan	First layer	0%	100%	0%	100%	0%	100%
	Subsequent layer	0%	100%	0%	100%	0%	100%
Side fan	First layer	0%	0%	0%	30-40%	0%	30-40%
	Subsequent layer	0%	7-10%	10-15%	50-55%	10-15%	50-55%

The result showed that fans speed settings varied for sample and test specimens printing. Pure HDPE had relatively lower thermal conductivity and slower crystallization, requiring minimal cooling to maintain adequate interlayer adhesion and prevent warping. While the Gd_2O_3 fillers enhanced heat dissipation and faster solidification, allowing for more cooling. Furthermore, the test specimens printing focused more on geometrical accuracy and repeatability with high printing quality; therefore, more cooling were applied.

The Table 8 below illustrates the adjustment process during the printing of samples and test specimens. HDPE-based materials showed relatively low stiffness, high shrinkage, and severe warping during printing, which increased the challenges of the fabrication process.

Table 8. Illustration of adjustment process of 3D printing HDPE/5%Gd_2O_3 samples

Description	Adjustment	Illustration
Distortion happened and failed layer adhesion	Reduced nozzle and printing temperature	
First few layers had good adhesions while remaining layers overheated	Further reduced nozzle and printing temperature, also turned on the fans for cooling	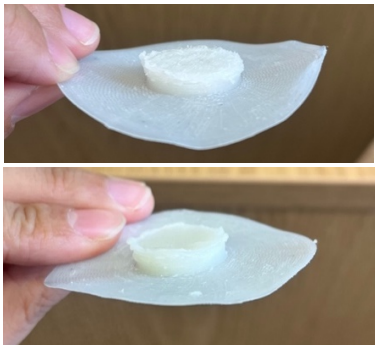
Clear layer structure form, however, shrinkage happened due to thermal contraction (side and bottom)	Slightly reduced the fans speed	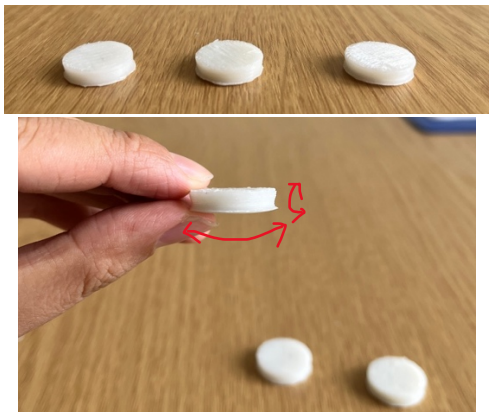
Uniform and smooth layer formed with 100% infill		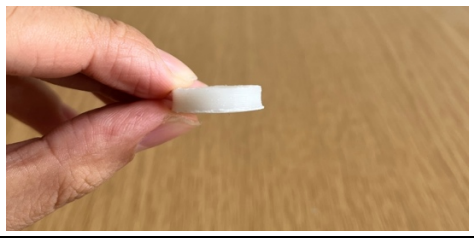

Controlling the printing temperature, nozzle temperature, and speed of the fans played an essential role for improving the printing quality of HDPE-based material (Table 9). Furthermore, significant warping was observed during the fabrication of test specimens of HDPE-based materials, because poor adhesion increased the edge lifting. Increasing the width of the brim was shown to effectively reduce warping and improved overall printing stability. Also, the ironing function was found to be unsuitable for HDPE-based materials because it caused overheating during fabrication. Since HDPE is highly sensitive to temperature, additional heat reduced the print quality.

Table 9. Illustration of adjustment process of 3D printing HDPE test specimens

Description	Adjustment	Illustration
Ironing was applied resulting overheated and failed layer adhesion	Turn off ironing	
Warping happened in the edge of brim, and poor interlayer adhesion	Increased the width of the brim and reduce the printing temperature	 
Warping reduced, but pillowing issue occurred (uneven surface or holes displayed causing non 100% infill)	Reduced printing temperature and speed	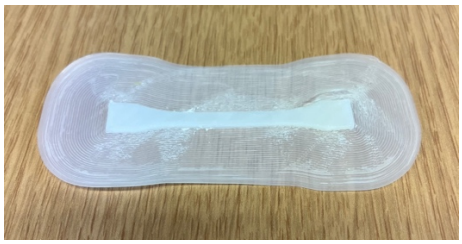
Perfect layer uniformity with 100% infill		 

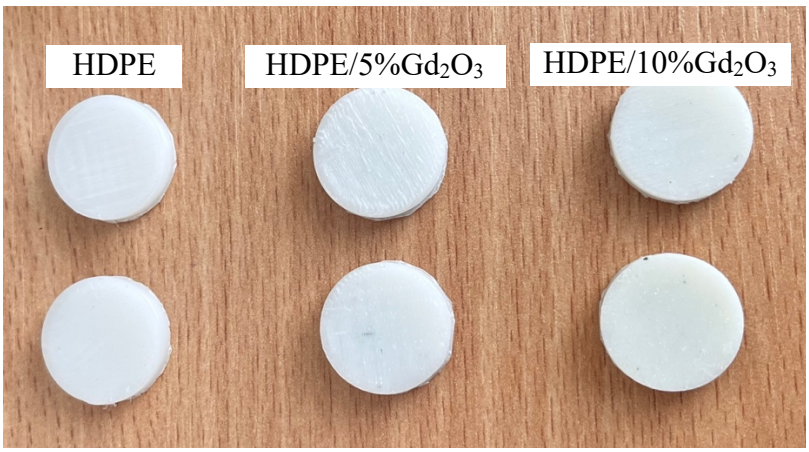

Fig. 35. Printed samples

Using the same printing temperature, speed, and fan parameters applied for the mechanical test specimens, cylindrical samples were 3D printed for radiation attenuation measurements. The use of identical printing parameters ensured reproducibility under the same processing conditions, despite differences in sample geometry (Figure 35).

Table 10. Comparison between theoretical density and measured density

Material	**Theoretical Density (g/cm^3)**	**Average measured Density (g/cm^3)**	**Percentage difference (%)**
HDPE	0.95	0.93	- 2.11
HDPE/5%Gd_2O_3	0.99	0.94	- 5.05
HDPE/10%Gd_2O_3	1.04	0.97	- 6.73

The Table 10 presents a comparison between the theoretical and measured densities. The density percentage difference (%) ranged from 2.11 – 6.73%, whith HDPE sample having the smallest density difference, while HDPE/10%Gd_2O_3 had the highest density difference. This indicated that the discrepancy increased with filler concentration, because of the voids created during 3D printing. The air gaps and incomplete fusion between layers reduced the actual density. This was expected, as Gd_2O_3 filament was more textured at higher Gd_2O_3 concentrations, which increased the viscosity and affected the interlayer adhesion during 3D printing process. Also, the Gd_2O_3 particles tended to cluster at higher filler concentrations, which caused uneven distribution during filament production and 3D printing, and air might trapped in the sample. This showed the challenge of fabricating HDPE-based material samples, and the importance of optimizing the parameters to minimize the density loss during 3D printing and filament production.

3.3. Mechanical tests

3.3.1. Tensile test

In this report, five test specimens were fabricated from each material for the tensile test: two were irradiated, and three were not irradiated, as illustrated in Figure 36. All of them followed the ISO 527-2 type 1BA standard for test specimens.

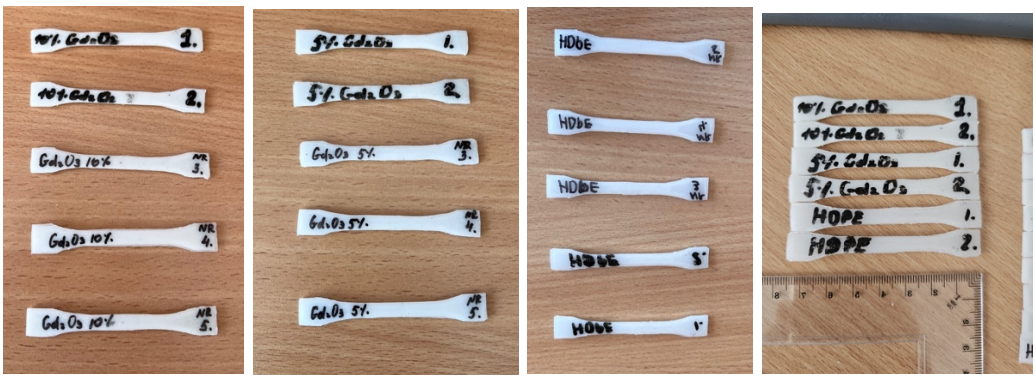

Fig. 36. Printed test specimens of different materials

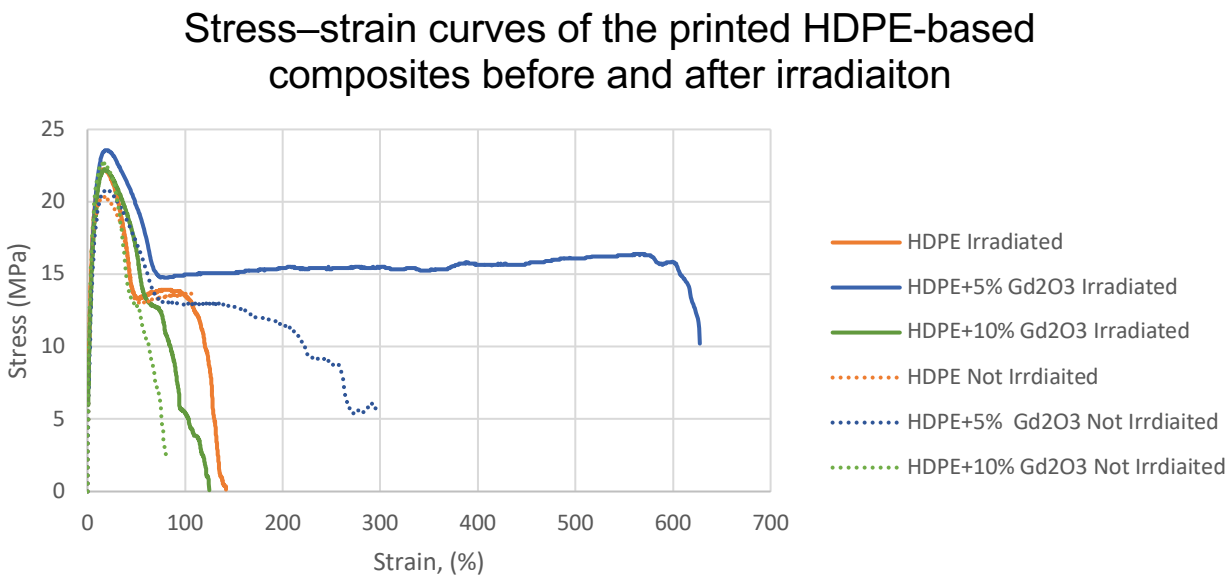

Fig. 37. Stress–strain curves of the printed HDPE-based composites before and after irradiation

The results in Figure 37 demonstrated that the Gd_2O_3 filler influenced the tensile behavior of HDPE composites. Before irradiation, all of them exhibited a distinct yield peak at approximately 22 MPa stress. The 5% Gd_2O_3 filler showed a noticeable increased peak stress at around 24 MPa. However, increasing the Gd_2O_3 filler concentration to 10% did not further improve strength. For the post-yield behavior, 5% Gd_2O_3 filler demonstrated remarkable enhancement in toughness (strain at break 627.33%), indicating that a 'bridging' effect occurred. Then, a reduction in ductility was observed, which may indicate an embrittlement effect. This behavior was possibly due to the high filler concentration, which

may have promoted micro-void formation and contributed to premature failure of the composite material.

After irradiation, the HDPE exhibited a yield point at approximately 20 MPa, and the peak stress slightly increased with higher filler concentration, with the 10% Gd_2O_3 filler recording a stress of 23 MPa. This indicates that Gd_2O_3 could slightly restrict chain mobility and enhance the stiffness of the polymer matrix. For the post-yield region, HDPE/5% Gd_2O_3 showed an extended elongation phase with high ductility (strain at break 295.20%). A significant reduction in ductility was observed for HDPE/10% Gd_2O_3, which showed more brittle behavior.

In general, the stress–strain curves showed that irradiation slightly decreased the mechanical performance of HDPE-based composites. Before irradiation, the samples, especially those with Gd_2O_3, exhibited higher tensile strength and elongation. After irradiation, both pure HDPE and HDPE/Gd_2O_3 became more brittle, with lower stress and strain at break. Increasing Gd_2O_3 content from 5% to 10% further reduced flexibility but helped maintain structural stability under irradiation.

Table 11 presents the tensile test results, including the measured properties of tensile strength, Young's modulus, stress at maximum load, and nominal strain at break.

Table 11. Tensile test result

Material	Status	Modulus (Young's Tensile) [GPa]	Stress at Maximum Load [MPa]	Strain at Break [%]
HDPE	Not Irradiated	0,9801	22,25	142,30
HDPE + 5% Gd2O3	Not Irradiated	0,9046	23,58	627,33
HDPE + 10% Gd2O3	Not Irradiated	1,0487	22,33	73,87
HDPE	Irradiated	1,1972	20,33	108,70
HDPE + 5% Gd2O3	Irradiated	0,7777	20,83	295,20
HDPE + 10% Gd2O3	Irradiated	1,1718	22,67	80,60

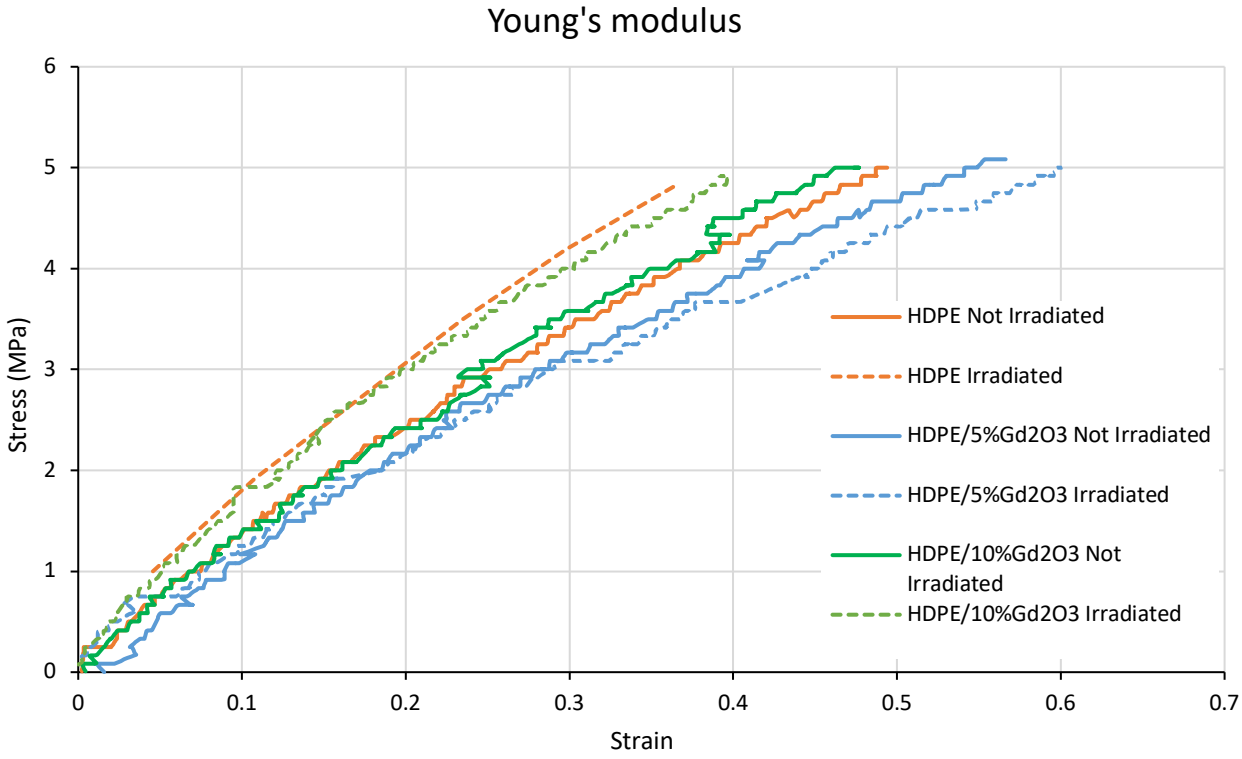

Fig. 38. Young's modulus of the printed HDPE-based composites before and after irradiation

Figure 38 shows the stress–strain curves made for comparison of Young's modulus of pure HDPE and HDPE/Gd_2O_3 composites before and after irradiation. Young's modulus was determined from the slope of the initial linear elastic region of the stress–strain curves. Higher modulus values indicate greater resistance to elastic deformation.

After irradiation, pure HDPE showed an increase in Young's modulus from 0.9801 GPa to 1.1972 GPa, indicating that irradiation enhanced the stiffness of the polymer. A similar trend was observed for the HDPE/10%Gd_2O_3 composite, where the modulus increased from 1.0487 GPa to 1.1718 GPa after irradiation. This may contribute to the filler reinforcement and irradiation effect, therefore the mechanical stiffness improved. In contrast, the irradiated HDPE/5%Gd_2O_3 composite exhibited a decrease in Young's modulus from 0.9046 to 0.7777 GPa. This reduction indicates a decrease in material stiffness and a lower resistance to elastic deformation compared with the non-irradiated sample. Therefore, this mechanical response should be carefully considered if this filler concentration is selected for future shielding applications.

In summary, the results demonstrate that both Gd_2O_3 incorporation and irradiation significantly influenced the elastic properties of the HDPE composites. Among all samples, the irradiated HDPE and irradiated HDPE/10%Gd_2O_3 composites exhibited the highest Young's modulus values, indicating superior stiffness and resistance to elastic deformation.

3.3.2. Theoretical radiations attenuation properties

Neutron attenuation properties

NGCal simulation was used to calculate the theoretical mass attenuation factor for thermal (25.4 meV) and fast neutrons (4 MeV).

Sample ID	Mass attenuation factor, cm ^{2}/g	
	Neutrons	
	Thermal (25,4 meV)	Fast (4 MeV)
HDPE	6,920	6,891
HDPE/5%Gd2O3	14,856	6,572
HDPE/10%Gd2O3	22,791	6,253

Fig. 39. NGCal simulation results of neutron mass attenuation

The results in Figure 39 shows that the mass attenuation factor increased dramatically with increasing Gd_2O_3 filler concentration for thermal neutrons because Gd has a high neutron capture cross section for thermal neutron capture. Meanwhile, the mass attenuation factor slightly decreased for fast neutrons because the hydrogen concentration decreased with the addition of Gd_2O_3 filler. This can be explained by the poor fast-neutron moderation capability of Gd compared with pure HDPE, while Gd has superior thermal-neutron absorption capability. The thermal neutron attenuation factor for HDPE/Gd_2O_3 composites has shown in Figure 40.

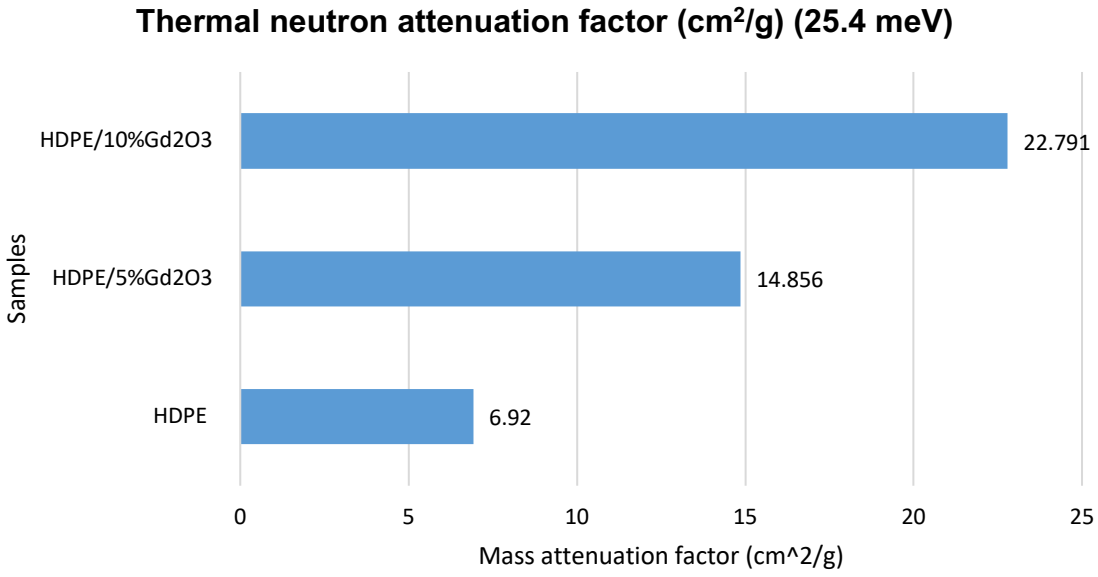

Fig. 40. Thermal neutron attenuation factor for HDPE/Gd_2O_3 composites

The NGCal calculations considered the combined effects of incoherent scattering and absorption for the relevant energies of thermal and fast neutrons, as well as the sum of

Compton scattering, photoelectric absorption, and pair production for the corresponding photon energies. Although this approach does not represent a direct mass attenuation calculation, it provides valuable comparative information. To complement this analysis, additional simulations were performed using the PHY-X/PDS software at a neutron energy of 4 MeV [52]. The results showed a fast neutron removal cross-section of approximately 0.122 cm^{-1}, with only small variations among the three samples. The respective material densities and weight fractions were included in the calculation.

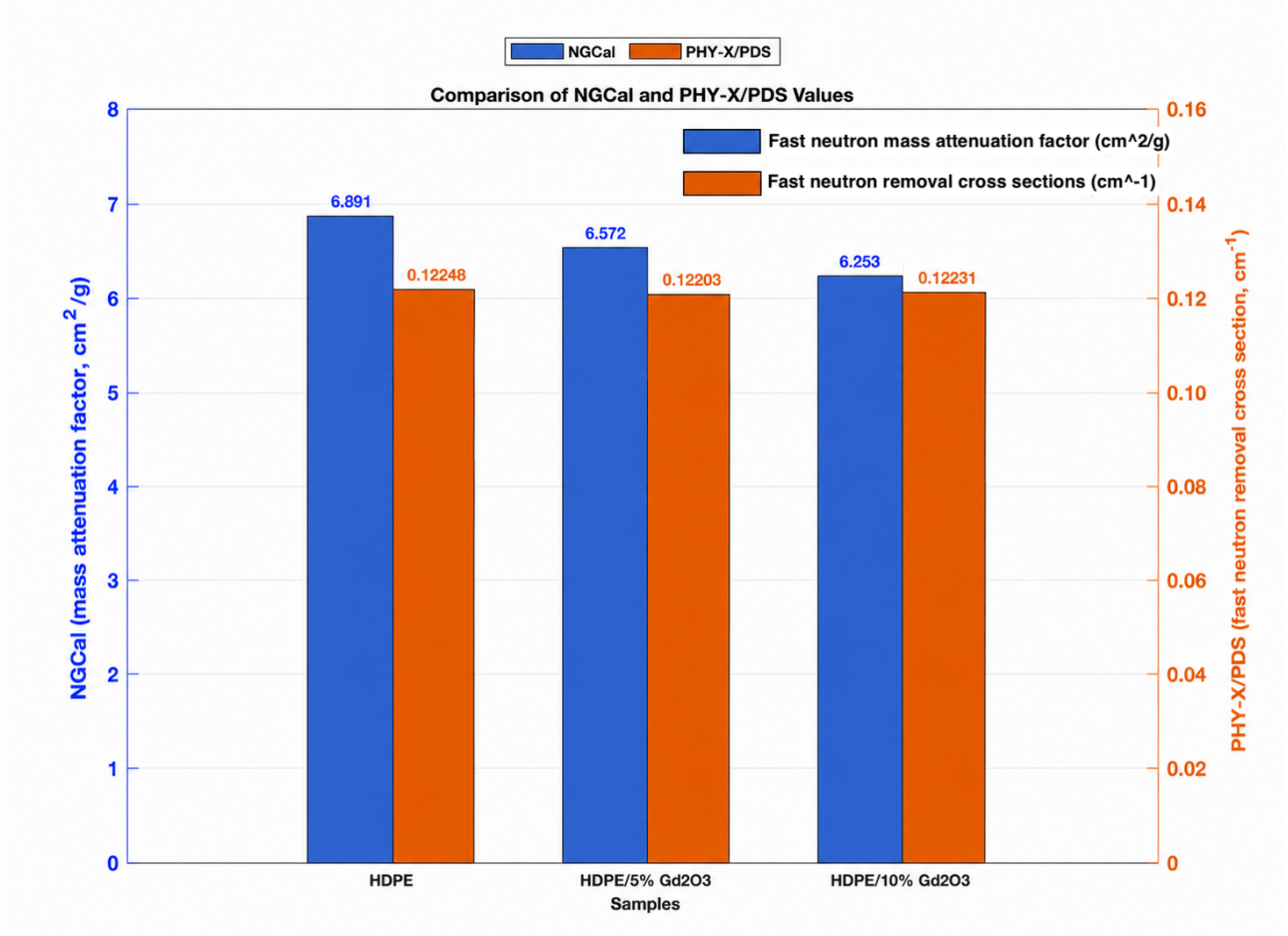

Fig. 41. Fast neutron parameters of HDPE/Gd_2O_3 composites

Figure 41 presents different fast neutron parameters of the HDPE/Gd_2O_3 composites, including the fast neutron mass attenuation factors obtained from NGCal and the fast neutron removal cross sections (FNRCS) obtained from PHY-X/PDS. According to the PHY-X/PDS analysis, the fast neutron removal cross section values remained nearly constant at approximately 0.122 cm^{-1} for all samples at a neutron energy of 4 MeV. The FNRCS were very similar because HDPE remained the main component in all composites and still provided most of the fast neutron moderation due to its high hydrogen content.

The NGCal results showed that the fast neutron mass attenuation factors for HDPE, HDPE/5% Gd_2O_3, and HDPE/10% Gd_2O_3 were 6.891, 6.572, and 6.253 cm^2/g, respectively. This confirms that Gd_2O_3 addition does not significantly improve fast neutron attenuation. Although Gd_2O_3 is not very effective for fast neutron moderation, its addition increased the material density, which slightly increased the probability of neutron interactions and helped maintain similar values for FNRCS.

Photon attenuation properties

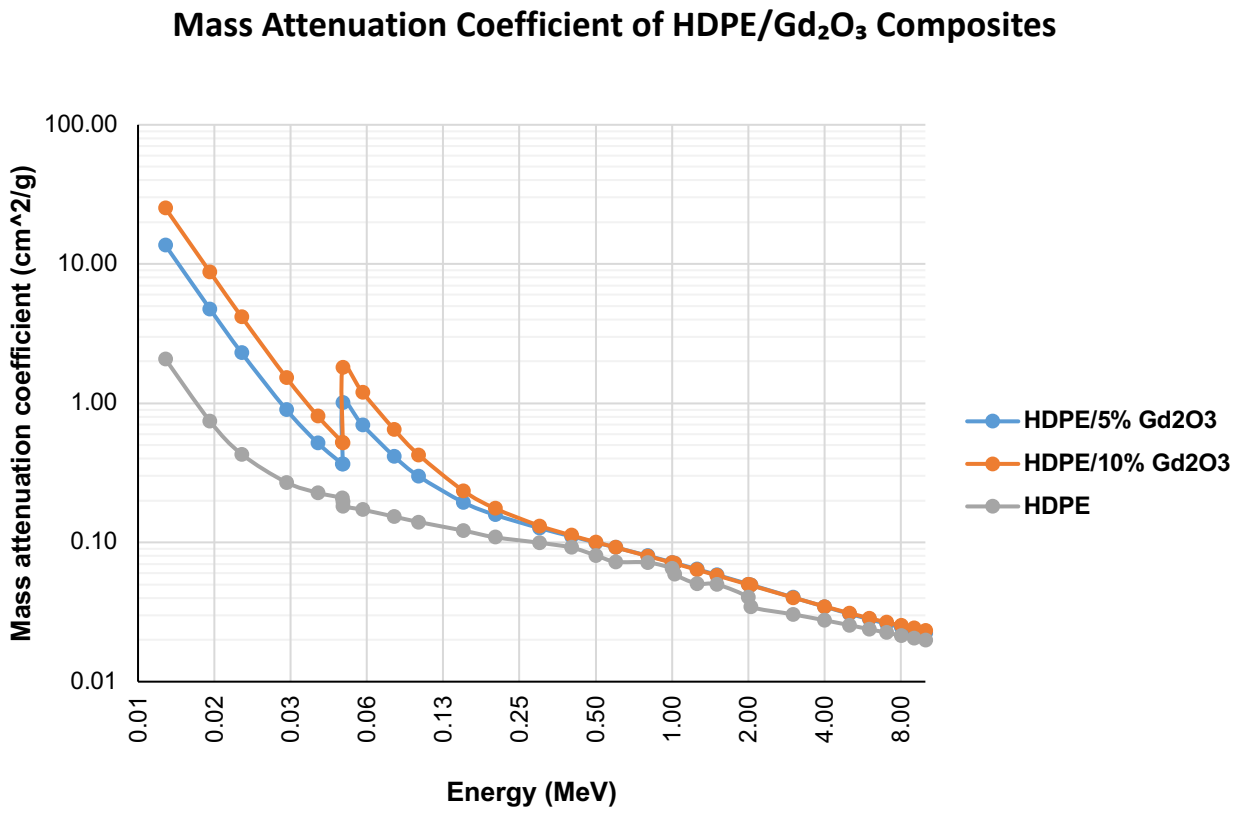

Fig. 42. Mass attenuation coefficient of HDPE/Gd_2O_3 composites

Figure 42 illustrates the mass attenuation coefficient of HDPE/Gd_2O_3 composites across the photon energy range of 0.01–8 MeV. The data demonstrates that the incorporation of Gd_2O_3 into the HDPE matrix enhances the material's radiation shielding capability, particularly within the low-energy region. Specifically, the mass attenuation coefficient increases as the Gd_2O_3 concentration increases from 5% to 10%, indicating a direct correlation between filler concentration and radiation attenuation efficiency. A notable feature in the attenuation spectrum is the "edge," observed at 50.2 keV, which corresponds to the K-edge of gadolinium. This abrupt increase in the mass attenuation coefficient is attributed to K-shell photoelectric absorption. This phenomenon occurs when the incident photon energy matches or exceeds the binding energy of K-shell electrons in gadolinium atoms, enabling direct ejection of inner-shell electrons through the photoelectric effect. This resonant absorption mechanism represents a critical energy threshold above which the composite material's shielding effectiveness undergoes a significant enhancement. Another important energy region is around 180–200 keV, which is relevant for gadolinium-containing composites because thermal neutron capture by gadolinium isotopes can produce characteristic gamma emissions in this range. In particular, strong gamma-ray intensities around 181 keV and 199 keV are associated with neutron capture reactions involving ^{155}Gd and ^{157}Gd isotopes. Therefore, the mass attenuation coefficient of HDPE/Gd_2O_3 composites in this energy range is important for evaluating their ability to attenuate secondary photons generated after thermal neutron absorption. As shown in the graph, the addition of Gd_2O_3

increases the mass attenuation coefficient compared with pure HDPE in this region, indicating improved attenuation of these capture-related photons.

3.3.3. Attenuation properties of experimental samples

10 samples were irradiated and analyzed: three 5mm-thick HDPE samples, three 1cm-thick of HDPE samples, two 5mm-thick HDPE/5%Gd_2O_3 samples, and two 5mm-thick HDPE/10%Gd_2O_3 samples. The average transmission and attenuation values were calculated and results are shown in Figure 43.

	Average Transmission	Average Attenuation (%)
HDPE 5 mm	0.839	16.09
HDPE 10 mm	0.735	26.52
HDPE/5%Gd2O3 5mm	0.900	10.01
HDPE/10%Gd2O3 5mm	0.847	15.34

Fig. 43. Average transmission and attenuation percentage results of samples in EBT3 film

The average attenuation of the HDPE sample increased from 16.09% for 5 mm to 26.52% for 1 cm. The results showed that the radiation attenuation properties of HDPE-based composites were strongly dependent on thickness and composition. The increasing of the thickness of pure HDPE material caused a higher reduction in transmission in EBT3 film measurements.

The incorporation of Gd_2O_3 in HDPE also affected the shielding characteristics. The HDPE/10% Gd_2O_3 sample reached an attenuation of 15.34%, compared to 10.01% for the HDPE/5% Gd_2O_3 sample. The result showed that HDPE/10% Gd_2O_3 generally produced better average attenuation performance than HDPE/5% Gd_2O_3.

Figure 44 presents the comparison of the average attenuation percentage for 5 mm HDPE/ Gd2O3 composite samples measured using EBT3 film. The attenuation increased in the order of HDPE/5%Gd2O3, HDPE/10%Gd2O3, and pure HDPE, with measured values of 10.01%, 15.34%, and 16.09%, respectively. This trend indicates that the attenuation behavior observed using the EBT3 films was influenced not only by neutron absorption, but also by the mixed-field radiation environment and the contribution of secondary gamma radiation generated during neutron capture interactions.

Several factors may have influenced the experimental attenuation results obtained using the EBT3 film in the mixed neutron–photon radiation field. First, the irradiation environment consisted of both neutron and photon components; therefore, the attenuation measured by the EBT3 films does not represent pure neutron attenuation alone. Since radiochromic films primarily respond to absorbed dose, the recorded signal includes contributions from neutrons, photons, and secondary radiation generated during neutron interactions within the shielding material.

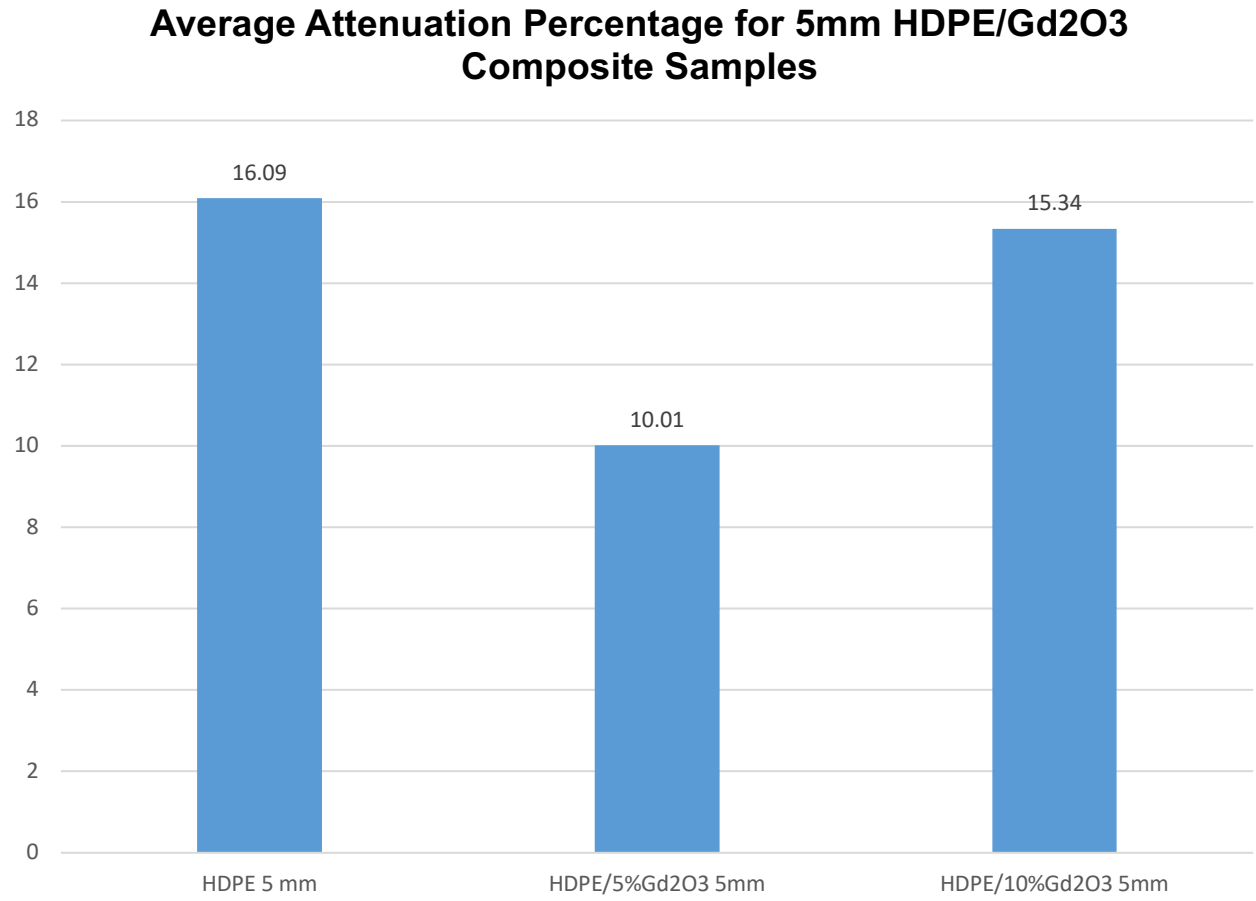

Fig. 44. Average attenuation percentage for printed HDPE/Gd_2O_3 composite samples

Second, the neutron detection mechanism of EBT3 films is also an important consideration. Unlike dedicated neutron detectors, EBT3 films do not directly detect neutrons; instead, their response is mainly caused by secondary charged particles and photons produced through neutron interactions [53].

Furthermore, the lower attenuation observed for the Gd_2O_3-containing composites does not necessarily indicate weaker shielding performance. Since EBT3 films measure the combined dose from neutrons, photons, and secondary radiation, the recorded attenuation is influenced by the mixed-field response. Gd_2O_3 enhances thermal neutron capture due to the high neutron absorption cross-section of gadolinium; however, this interaction can also produce secondary gamma radiation, which may contribute to the dose recorded by the film. Therefore, the lower attenuation value may partly reflect increased thermal neutron capture accompanied by secondary photon production, rather than reduced neutron shielding ability. In contrast, the higher attenuation observed for pure HDPE is likely related mainly to fast neutron moderation and scattering by hydrogen in the HDPE matrix. Future work should therefore investigate the use of additional photon-attenuating layers to reduce capture-related secondary gamma radiation. In addition, dedicated neutron detectors should be considered to separate the neutron contribution from the total mixed-field dose.

Conclusions

1. HDPE reinforced Gd_2O_3 composite filaments were successfully produced. The heater temperature and fan speed were carefully controlled during the extrusion process. Pure HDPE filament exhibited greater transparency, smoother surface and higher flexibility compared to filaments incorporated with Gd_2O_3 fillers. While HDPE composite filaments filled with 5 wt% and 10 wt% Gd_2O_3 demonstrated relatively higher stiffness, slightly textured surface, and lower transparency.
2. HDPE reinforced Gd_2O_3 composite samples were successfully fabricated, including pure HDPE, HDPE/5 wt% Gd_2O_3, and HDPE/10 wt% Gd_2O_3, with measured density of 0.93, 0.94, and 0.97 g/cm^3, respectively. The percentage difference between theoretical and measured densities ranged from 2.11 to 6.73%, with the pure HDPE sample exhibiting the smallest density deviation, while HDPE/10%Gd_2O_3 demonstrated the largest density difference.
3. The tensile test was performed using printed ISO 527-2 type 1BA test specimens. The results demonstrated that Gd_2O_3 filler influenced the tensile behavior of HDPE composites. All the specimens exhibited a distinct yield peak at a stress of approximately 22 MPa. Among all samples, the irradiated HDPE and irradiated HDPE/10%Gd_2O_3 composites exhibited the highest Young's modulus values, indicating superior stiffness and resistance to elastic deformation.
4. The EBT3 film measurements demonstrated the mixed-field attenuation behavior of HDPE/Gd_2O_3 composites. Pure HDPE showed the highest measured attenuation, mainly due to fast neutron moderation and scattering by hydrogen, while Gd_2O_3 addition contributed to thermal neutron capture and the possible production of secondary photons.
5. Obtained results indicate the potential use of HDPE+Gd_2O_3 composites as lead-free, lightweight shielding materials for LINAC head shielding applications.

List of references

1. MIYASAKA, Ryohei, CHO, SangYong, HIRAOKA, Takuya, CHIBA, Kohei, KAWACHI, Toru, KATAYOSE, Tetsurou, SUDA, Yuhi and HARA, Ryusuke. Investigation of halcyon multi-leaf collimator model in Eclipse treatment planning system: A focus on the VMAT dose calculation with the Acuros XB algorithm. *Journal of Applied Clinical Medical Physics*. 9 January 2022. Vol. 23, no. 3. DOI 10.1002/acm2.13519.

2. MARTNEZ OVALLE, S. Agustn. Neutron dose equivalent in tissue due to linacs of clinical use. *Frontiers in Radiation Oncology*. 3 July 2013. DOI 10.5772/56513.

3. MA, A., AWOTWI-PRATT, J., ALGHAMDI, A., ALFURAIH, A. and SPYROU, N. M. Monte Carlo Study of Photoneutron production in the Varian Clinac 2100C LINAC. *Journal of Radioanalytical and Nuclear Chemistry*. 24 November 2007. Vol. 276, no. 1, p. 119–123. DOI 10.1007/s10967-007-0419-3.

4. SOHRABI, Mehdi and HAKIMI, Amir. Novel 6 MV X-ray photoneutron detection and dosimetry of medical accelerators. *Physica Medica*. April 2017. Vol. 36, p. 103–109. DOI 10.1016/j.ejmp.2017.03.020.

5. HORST, Felix, FEHRENBACHER, Georg and ZINK, Klemens. On the neutron radiation field and air activation around a medical electron linac. *Radiation Protection Dosimetry*. 11 May 2016. DOI 10.1093/rpd/ncw120.

6. KHABAZ, Rahim. Effect of each component of a linac therapy head on neutron and Photon Spectra. *Applied Radiation and Isotopes*. September 2018. Vol. 139, p. 40–45. DOI 10.1016/j.apradiso.2018.04.022.

7. SHABIB, Mohamed, TAWFIK, Eman. K., REHEEM, A. M., NADA, Afaf and ASHRY, H. A. A comparative analysis of Gamma and neutron radiation shielding properties of gd2o3 nanoparticles within HDPE composites irradiated with argon ion beam. *Scientific Reports*. 11 March 2026. Vol. 16, no. 1. DOI 10.1038/s41598-026-40153-x.

8. BANAEE, Nooshin, GOODARZI, Kiarash and NEDAIE, Hassan Ali. Neutron contamination in Radiotherapy Processes: A review study. *Journal of Radiation Research*. 31 August 2021. DOI 10.1093/jrr/rrab076.

9. POLACZEK-GRELIK, Kinga, KAWA-IWANICKA, Aneta, RYGIELSKI, Marek and MICHALECKI, Łukasz. Gamma radiation in the vicinity of the entrance to Linac Radiotherapy Room. *Use of Gamma Radiation Techniques in Peaceful Applications*. 2 October 2019. DOI 10.5772/intechopen.82726.

10. UDDIN, M. F., AHASAN, M. M., KHATUN, R., AKTER, S., JAMIL, H. M., MONIKA, A. N. and RAHMAN, M. A. Shielding design basis and its calculation of high energy medical linac installed in Bangladesh Atomic Energy Commission, Bangladesh. *Universal Journal of Medical Science*. November 2017. Vol. 5, no. 2, p. 27–31. DOI 10.13189/ujmsj.2017.050202.

11. ALMATANI, Turki and HUGTENBURG, Richard P. Evaluation of lead shielding against head leakage from a 6 MV Agility Linac using Fluka Monte Carlo Simulation. *Radiation Physics and Chemistry*. December 2025. Vol. 237, p. 112974. DOI 10.1016/j.radphyschem.2025.112974.

12. OLIVEIRA, Alex C H, VIEIRA, José W, SANTANA, Marcelo G and LIMA, Fernando R AOLIVEIRA, Alex C H, VIEIRA, José W, SANTANA, Marcelo G and LIMA, Fernando R A. MONTE CARLO SIMULATION OF A MEDICAL LINEAR ACCELERATOR FOR GENERATION OF PHASE SPACES,2013.ISBN 978-85-99141-05-2 .

13. *Handbook of radiotherapy physics: theory and practice*. . MAYLES, Philip, NAHUM, Alan E. and ROSENWALD, Jean-Claude (eds.). 2007 ISBN 978-0-7503-0860-1R896.7 .H36 2007.

14. GAO, Song, CIBRIAN, Andres, OHRT, Jared and BALTER, Peter. Detection of the linac jaw face angle misalignment using high energy electron beam symmetry. *Journal of Applied Clinical Medical Physics*. December 2025. Vol. 26, no. 12. DOI 10.1002/acm2.70419.

15. NATH, Ravinder, BOYER, Arthur L., RIVIERE, Philip D. La, MCCALL, Richard C. and PRICE, Kenneth W.NATH, Ravinder, BOYER, Arthur L., RIVIERE, Philip D. La, MCCALL, Richard C. and PRICE, Kenneth W. *Neutron Measurements Around High Energy X-Ray Radiotherapy Machines* Online. AAPM, 1986. Accessed 2 April 2026. .

16. *Structural shielding design and evaluation for medical use of X-rays and gamma rays of energies up to 10 MeV: recommendations of the National Council on Radiation Protection and Measurements*. NATIONAL COUNCIL ON RADIATION PROTECTION AND MEASUREMENTS, 1976. ISBN 978-0-913392-31-7RA975.5.R3 N37 1976a.

17. BLIDEANU, V., BESNARD-VAUTERIN, C., HORVÁTH, D., LEFEBVRE, B., SALVAT-PUJOL, F. and VERSACI, R. Neutron spectra from Photonuclear Reactions: Performance testing of Monte-Carlo Particle Transport Simulation codes. *Nuclear Instruments and Methods in Physics Research Section B: Beam Interactions with Materials and Atoms*. April 2024. Vol. 549, p. 165292. DOI 10.1016/j.nimb.2024.165292.

18. ZABIHINPOOR, Seyedmohammad and HASHEMINIA, MaryamZABIHINPOOR, Seyedmohammad and HASHEMINIA, Maryam. Calculation of Neutron Contamination from Medical Linear Accelerator in Treatment Room. Adv. Studies Theor. Phys., Vol. 5, 2011, no. 9, 421 - 428. .

19. UDDIN, Md Fakhar, AKTER, Shirin, AHMED, Mahiuddin, SATTAR, Bushra Nufrin, MORSHED, K.M. Mahabub, OSMAN, Hamid, BOKHARI, Fawzi F., ALSUFYANI, Sultan J., ISSA, Shams A.M. and KHANDAKER, Mayeen Uddin. Photoneutron production mechanisms, their characteristics, and shielding strategies in high-energy LINAC environment: A Review. *Journal of Radiation Research and Applied Sciences*. September 2024. Vol. 17, no. 3, p. 101031. DOI 10.1016/j.jrras.2024.101031.

20. FACURE, A., DA SILVA, A. X., DA ROSA, L. A., CARDOSO, S. C. and REZENDE, G. F. On the production of neutrons in laminated barriers for 10 MV Medical Accelerator Rooms. *Medical Physics*. 24 June 2008. Vol. 35, no. 7Part1, p. 3285–3292. DOI 10.1118/1.2940192.

21. HOWELL, Rebecca M., KRY, Stephen F., BURGETT, Eric, HERTEL, Nolan E. and FOLLOWILL, David S. Secondary neutron spectra from modern Varian, Siemens, and

Elekta Linacs with Multileaf collimators. *Medical Physics*. 12 August 2009. Vol. 36, no. 9Part1, p. 4027–4038. DOI 10.1118/1.3159300.

22. BRKIC, Hrvoje, KASABASIC, Mladen, IVKOVIC, Ana, AGIC, Dejan, KRPAN, Ivana and FAJ, Dario. Influence of head cover on the neutron dose equivalent in Monte Carlo simulations of High Energy Medical Linear Accelerator. *Nuclear Technology and Radiation Protection*. 2018. Vol. 33, no. 2, p. 217–222. DOI 10.2298/ntrp1802217b.

23. KINSARA, Abdulraheem and EL GIZAWY, Ahmed Sherif. Review of leakage from a linear accelerator and its side effects on cancer patients. *Journal of Nuclear Medicine & Radiation Therapy*. 2016. Vol. 07, no. 03. DOI 10.4172/2155-9619.1000288.

24. TAYLOR, MichaelL and KRON, Tomas. Consideration of the radiation dose delivered away from the treatment field to patients in radiotherapy. *Journal of Medical Physics*. 2011. Vol. 36, no. 2, p. 59. DOI 10.4103/0971-6203.79686.

25. KRY, Stephen F., BEDNARZ, Bryan, HOWELL, Rebecca M., DAUER, Larry, FOLLOWILL, David, KLEIN, Eric, PAGANETTI, Harald, WANG, Brian, WUU, Cheng-Shie and GEORGE XU, X. AAPM tg 158: Measurement and calculation of doses outside the treated volume from external-beam radiation therapy. *Medical Physics*. 20 August 2017. Vol. 44, no. 10. DOI 10.1002/mp.12462.

26. UMM-E-KULSOOM, GURSAL, Shakaib Arslan, KHURSHID, Muhammad Shahbaz, SAIF-UR-REHMAN, Malik, MINHAS, Awais Shahid, YASIN, Tariq, MEHBOOB, Nasir and MEHMOOD, Malik Sajjad. Investigating the effect of adding CDO nano particles on neutron shielding efficacy of HDPE. *Radiation Physics and Chemistry*. December 2020. Vol. 177, p. 109145. DOI 10.1016/j.radphyschem.2020.109145.

27. ALHARBI, Ahmed, ASEMI, Nassar N. and ALNAGRAN, Hamed. Hybrid phy-X/PSD–GEANT4 assessment of Gamma and neutron shielding in lead-free HDPE composites reinforced with high-Z oxides. *Polymers*. 9 January 2026. Vol. 18, no. 2, p. 179. DOI 10.3390/polym18020179.

28. SAENBOONRUANG, Kiadtisak, POLTABTIM, Worawat, THUMWONG, Arkarapol, PIANPANIT, Theerasarn and RATTANAPONGS, Chanis. Rare-earth oxides as alternative high-energy photon protective fillers in HDPE composites: Theoretical aspects. *Polymers*. 10 June 2021. Vol. 13, no. 12, p. 1930. DOI 10.3390/polym13121930.

29. DURFEE, William K. and IAIZZO, Paul A.DURFEE, William K. and IAIZZO, Paul A. Medical Applications of 3D Printing. In : *Engineering in Medicine*. Online. Elsevier, 2019. p. 527–543. Accessed 24 April 2026. ISBN 978-0-12-813068-1.

30. ALAMRI, Nawaf Mohammad, PACKIANATHER, Michael and BIGOT, Samuel. Predicting the porosity in selective laser melting parts using hybrid regression convolutional neural network. *Applied Sciences*. 8 December 2022. Vol. 12, no. 24, p. 12571. DOI 10.3390/app122412571.

31. BERGER, Christian, SCHIMO-AICHHORN, Gabriela, GRONAU, Stefan, SAFT, Franziska, SEIRINGER, Sarah and SCHEITHAUER, Uwe. Potential and challenges for powder bed fusion – laser beam (PBF-LB) in Industrial Ceramic Additive Manufacturing. *Open Ceramics*. June 2024. Vol. 18, p. 100614. DOI 10.1016/j.oceram.2024.100614.

32. TAO, Qi, FU, Boao and ZHONG, Fei. A review of challenges and future perspectives for high-speed material extrusion technology. *Applied Sciences*. 17 November 2025. Vol. 15, no. 22, p. 12176. DOI 10.3390/app152212176.

33. LEFAY, Catherine and GUILLANEUF, Yohann. Recyclable/degradable materials via the insertion of labile/cleavable bonds using a comonomer approach. *Progress in Polymer Science*. December 2023. Vol. 147, p. 101764. DOI 10.1016/j.progpolymsci.2023.101764.

34. ELKASEER, Ahmed, CHEN, Karin J., JANHSEN, Jan C., REFLE, Oliver, HAGENMEYER, Veit and SCHOLZ, Steffen G. Material jetting for Advanced Applications: A state-of-the-art review, gaps and Future Directions. *Additive Manufacturing*. December 2022. Vol. 60, p. 103270. DOI 10.1016/j.addma.2022.103270.

35. OLIVER, L., CANDELA-JUAN, C., PALMA, J.D., PUJADES, M.C., SORIANO, A., VILAR, J., MARTÍNEZ, J.M., MESTRE, V., RUIZ-RODRÍGUEZ, J.C. and LLORCA-DOMAICA, N. Comparison of the dosimetric response of 4-elements OSL and TL Passive Personal Dosimeters. *Radiation Measurements*. December 2017. Vol. 107, p. 128–135. DOI 10.1016/j.radmeas.2017.09.001.

36. BOROWICZ, Dorota Maria, MALICKI, Julian, MYTSIN, Gennady and SHIPULIN, Konstantin. Wax Boluses and accuracy of EBT and RTQA radiochromic film detectors in radiotherapy with the JINR Phasotron Proton Beam. *Reports of Practical Oncology & Radiotherapy*. January 2014. Vol. 19, no. 1, p. 12–18. DOI 10.1016/j.rpor.2013.05.007.

37. MCCABE, Bradley P., SPEIDEL, Michael A., PIKE, Tina L. and VAN LYSEL, Michael S. Calibration of gafchromic XR-RV3 radiochromic film for skin dose measurement using standardized x-ray Spectra and a commercial flatbed scanner. *Medical Physics*. 15 March 2011. Vol. 38, no. 4, p. 1919–1930. DOI 10.1118/1.3560422.

38. FARHOOD, Bagher, PARWAIE, Wrya, REFAHI, Soheila and ARDEKANI, MahdiehAfkhami. Different dosimeters/detectors used in small-field dosimetry: Pros and cons. *Journal of Medical Signals & Sensors*. 2018. Vol. 8, no. 3, p. 195. DOI 10.4103/jmss.jmss_3_18.

39. BOOTHROYD, Andrew T. *Principles of Neutron Scattering from Condensed Matter*. Online. 1 2020 ISBN 978-0-19-886231-4.

40. HENSKE, M., KLEIN, M., KÖHLI, M., LENNERT, P., MODZEL, G., SCHMIDT, C.J. and SCHMIDT, U. The 10b based Jalousie Neutron Detector – an alternative for 3HE filled position sensitive counter tubes. *Nuclear Instruments and Methods in Physics Research Section A: Accelerators, Spectrometers, Detectors and Associated Equipment*. September 2012. Vol. 686, p. 151–155. DOI 10.1016/j.nima.2012.05.075.

41. PEPLOWSKI, Patrick N., YOKLEY, Zachary W., LIEBEL, Madison, CHENG, Shuo, ELPHIC, Richard C., HOOGERHEIDE, Shannon F., LAWRENCE, David J. and NICO, Jeffrey S. Position-dependent neutron detection efficiency loss in 3HE gas proportional counters. *Nuclear Instruments and Methods in Physics Research Section A: Accelerators, Spectrometers, Detectors and Associated Equipment*. December 2020. Vol. 982, p. 164574. DOI 10.1016/j.nima.2020.164574.

42. UDDIN, Zaheer, YASIN, Tariq, SHAFIQ, Muhammad, RAZA, Asif and ZAHUR, Awais. On the physical, chemical, and neutron shielding properties of polyethylene/boron carbide

composites. *Radiation Physics and Chemistry*. January 2020. Vol. 166, p. 108450. DOI 10.1016/j.radphyschem.2019.108450.

43. RABEE BEHNAM ALKHAYAT. Simulation and analysis of the 3HE detector for thermal neutron detection. *Journal of Education and Science*. 1 June 2023. Vol. 32, no. 2, p. 45–50. DOI 10.33899/edusj.2023.138006.1322.

44. KOCHER, David C. Assessment of occupational exposure due to external sources of radiation. *Health Physics*. May 2000. Vol. 78, no. 5, p. 567–568. DOI 10.1097/00004032-200005000-00019.

45. DANIEL, Rotari, VALECA, Serban Constantin and ROTH, CsabaDANIEL, Rotari, VALECA, Serban Constantin and ROTH, Csaba. BONNER SPHERE NEUTRON SPECTROMETRY – NEUTRON SPECTROMETER CALIBRATION EXPERIMENTS. . 2019. .

46. RAMALHO, Eduardo and REINA, LuizRAMALHO, Eduardo and REINA, Luiz. BUBBLE DETECTOR'S EVALUATION FOR NEUTRON FIELD MEASUREMENTS IN A VERY KNOWN SOURCE. . 2011. .

47. AYUELA, A., MARCH, N. H. and KLEIN, D. J. Optimized geometry of the cluster Gd2O3 and proposed antiferromagnetic alignment of F-electron magnetic moment. *The Journal of Physical Chemistry A*. 20 September 2007. Vol. 111, no. 40, p. 10162–10165. DOI 10.1021/jp0745790.

48. Plastics — Determination of tensile properties Part 2: Test conditions for moulding and extrusion plastics. *BSI Standards Publication. BS-EN-ISO-527-2-2012-tensile-test-specimens*. 2012. ISBN 978 0 580 70623 3.

49. FURRER, A.FURRER, A. Neutron Sources. In : *Encyclopedia of Condensed Matter Physics*. Online. Elsevier, 2005. p. 69–75. Accessed 5 May 2026. ISBN 978-0-12-369401-0.

50. SCHIRMEISTER, Carl G., HEES, Timo, LICHT, Erik H. and MÜLHAUPT, Rolf. 3D printing of high density polyethylene by fused filament fabrication. *Additive Manufacturing*. August 2019. Vol. 28, p. 152–159. DOI 10.1016/j.addma.2019.05.003.

51. KOFFI, Agbelenko, TOUBAL, Lotfi, JIN, Minde, KOFFI, Demagna, DÖPPER, Frank, SCHMIDT, Hans-Werner and NEUBER, Christian. Extrusion-based 3D printing with high-density polyethylene birch-fiber composites. *Journal of Applied Polymer Science*. 18 November 2021. Vol. 139, no. 15. DOI 10.1002/app.51937.

52. OSMAN, Ahmed. Computational analysis of gamma-ray and fast neutron attenuation performance of some thorium and uranium compounds. *Brazilian Journal of Radiation Sciences*. 5 December 2025. Vol. 13, no. 4. DOI 10.15392/2319-0612.2025.2868.

53. ELMAGHRABY, Elsayed K., SALEH, Nourhan H., ABDELAAL, Saad and EL GHAZALY, M. Neutron and Gamma Dosimetry with Radiochromic Film. *Radiation Physics and Chemistry*. January 2026. Vol. 238, p. 113126. DOI 10.1016/j.radphyschem.2025.113126.